Magnetic resonance imaging methods in heterogeneous catalysis

Igor V. Koptyug[a,b]

DOI: 10.1039/9781782621485-00001

Applications of spatially resolved magnetic resonance in heterogeneous catalysis and related fields are considered. The chapter starts with a simple description of the basic principles of MRI and the discussion of the specific features which make MRI a powerful and versatile toolkit capable of providing useful and diverse information about catalysts, reactors and processes within them in a non-invasive manner. Next, practical aspects of constructing an MRI-compatible reactor are presented along with the methods for, and examples of, the structural MRI studies of packed beds, model reactors and related geometries. The basic principles of mass transport studies with NMR and MRI are considered next, and the literature examples of MRI studies of mass transport in model systems are briefly outlined. The rest of the chapter is devoted to the analysis of the studies of model catalytic reactors under operating conditions, and includes MRI studies of distribution and mass transport of fluids, spatially resolved spectroscopic studies of conversion, MRI thermometry of operating catalytic reactors and microreactors, and the use of the emerging techniques for nuclear spin hyperpolarization to boost the sensitivity of NMR and MRI in catalytic applications.

Downloaded from http://books.rsc.org/books/edited-volume/chapter-pdf/1688710/bk9781849739191-00001.pdf by guest on 03 October 2023

1 Introduction

Nuclear magnetic resonance imaging, abridged to ''MRI'' to stress its harmless nature, has become one of the most powerful instruments in modern medical diagnostics. In fact, MRI has revolutionized modern medicine by enabling physicians to literally see the state of internal organs in a human body and various processes taking place within it. This ability, coupled with the non-invasive nature of the technique, made it possible to abandon the ''black box'' approach, in which the diagnosis is often based on superficial observations and a limited number of symptoms which are often similar in many diseased states. The success of medial MRI might seem surprising given that the technique has modest spatial resolution and a number of significant limitations as compared to other modern imaging techniques, *e.g.* computer assisted (X-ray) tomography (CAT), positron emission tomography (PET), *etc.* However, the key feature of MRI is that it is best characterized as a versatile toolkit,[1] in contrast to many other techniques which are powerful but specialized tools. In addition to morphological studies, the medical MRI toolkit contains tools for angiography, thermometry, spectroscopy, elastography, functional MRI, and a lot more. The foundation for this tremendous diversity is the versatile nature of image contrast in MRI. The latter is sensitive to a wide range of properties of an

[a]*International Tomography Center, SB RAS, 3A Institutskaya St., Novosibirsk 630090, Russia*
[b]*Novosibirsk State University, 2 Pirogova St., Novosibirsk 630090, Russia. E-mail: koptyug@tomo.nsc.ru*

© The Royal Society of Chemistry 2014

object under study and processes taking place within it. Furthermore, image contrast in MRI can be deliberately tailored to the needs of a particular study. As a result, MRI is able to provide a lot more than just structural information. It is this ability which makes MRI so powerful a technique.

Unlike modern medicine, chemical and process engineering practice still largely relies on the ''black box'' approach, trying to figure out what is happening inside an operating reactor on the basis of a number of external measurements (pressure drop, temperature, chemical composition of the feed and reactor output, transient response curves, *etc.*). A number of modern imaging techniques are being developed to overcome the existing limitations, but so far our ability to see the inner works of one of the most sophisticated bioreactors – human body – by far exceeds our ability to visualize processes inside, *e.g.*, a packed bed reactor. In fact, biomedical MRI has reached the stage when metabolic processes taking place in the cells of various tissues and organs can be interrogated in live animals,[2] and this possibility is currently being extended to in-human studies.

With all this progress in biomedical MRI applications, it might seem surprising that MRI has not become a routine technique to ''diagnose'' the behavior of various chemical reactors. One of the obstacles on this way is the feature that makes MRI such a powerful technique – the diversity of image contrast mechanisms, *i.e.*, the sensitivity of the detected signal to a wide range of object properties. As a result, many MRI strategies developed in medical MRI to a state of perfection perform unsatisfactorily when applied to non-biological objects. At present, non-biomedical applications of MRI are still an art rather than routine studies despite the fact that the interest in such studies is clearly on the rise, including applications to problems related to catalysis.

2 The MRI technique

NMR in general and MRI in particular explore the interaction of nuclear spins with static and oscillating magnetic fields. In NMR spectroscopy, one acquires NMR spectra which characterize local magnetic environments of nuclei possessing a non-zero spin (*e.g.*, ^{1}H, ^{13}C, ^{19}F, ^{31}P) and thereby provide information on chemical composition of a sample, its molecular structure and dynamic transformations, *etc.* In an NMR spectrum, the position of a particular resonance (the resonance frequency ω) is proportional to the applied static magnetic field B_0 and the magnetogyric ratio γ of the magnetic nucleus under consideration ($\omega \propto \gamma B_0$). This implies that if, for instance, a container with water is placed in a spatially uniform magnetic field (Fig. 1a), a single NMR resonance will be observed in the NMR spectrum (Fig. 1b). Indeed, in NMR spectroscopy, high magnetic field homogeneity is essential to obtain high spectral resolution. In contrast, in MRI the magnetic field is intentionally made to depend on a spatial coordinate, often in a linear fashion (Fig. 1c). In this example, different volumes of water reside in different static magnetic fields and therefore produce NMR resonances at different

Downloaded from http://books.rsc.org/books/edited-volume/chapter-pdf/1688710/bk9781849739191-00001.pdf by guest on 03 October 2023

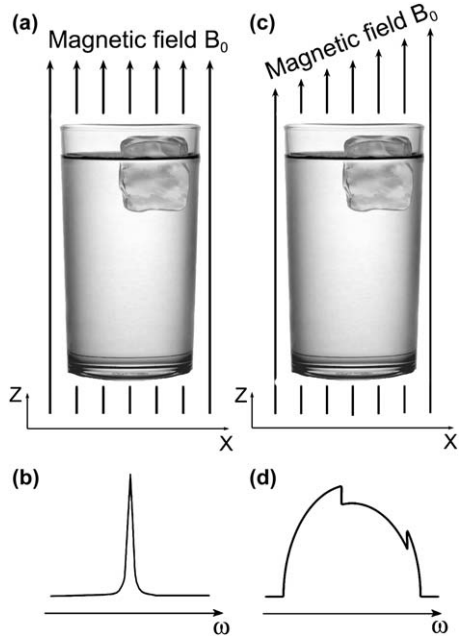

Fig. 1 A glass of water with an ice cube in a homogeneous magnetic field without (a) and with a superimposed magnetic field gradient along the x coordinate axis (c), and the expected ^{1}H NMR spectra (b,d). Usually, only liquid contributes to the detected signal. The 'spectrum' in (d) is essentially an integral projection of the sample on the x axis.

resonance frequencies. The resulting ''spectrum'' is essentially a one-dimensional integral projection of the sample on the direction of the gradient (Fig. 1d). If three orthogonal gradients are available, they can be combined to produce a resulting gradient with an arbitrary orientation in space, rendering an MRI measurement free from any orientational preferences and making possible the acquisition of 2D and 3D images. Gradients are often applied as pulses and are incorporated in an NMR pulse sequence along with radiofrequency pulses and delays. The borderline between MRI and non-imaging NMR applications is rather vague. Indeed, many modern magnetic resonance (MR) experiments combine spatial and spectral coordinates and are best described as experiments in a multidimensional (sub)space of spatial, spectral and temporal coordinates rather than MR spectroscopy or imaging.

NMR/MRI experiments require that a sample under study contains a large number of magnetic nuclei. Their nuclear spins serve as intrinsic probes or tracers which can convey the information about their spatial position, local environments and mobility of the groups of atoms and molecules they belong to, to the NMR detector which is usually placed externally with respect to the object under study. Therefore, an MRI experiment is non-invasive and non-destructive, does not require the introduction of any other tracers or probes into the object under study, and allows one to monitor various dynamic processes *in situ*, without a need to periodically interrupt them to make a measurement.

Downloaded from http://books.rsc.org/books/edited-volume/chapter-pdf/1688710/bk9781849739191-00001.pdf by guest on 03 October 2023

Modern NMR spectroscopy is performed with virtually all nuclei possessing a non-zero spin. In principle, an image can also be obtained using any nucleus with a non-zero spin. In practice, however, the majority of the MRI studies are performed using ^{1}H NMR signal detection, with a much smaller number of studies reported where other nuclei were addressed. The reason is that the sensitivity (signal-to-noise ratio, SNR) available in an experiment represents one of the major limitations for achieving better spatial resolution, implementing faster imaging strategies and developing more informative MRI applications. At the same time, the multinuclear capability of MRI is one of the highly promising directions for future developments, and the number of such applications is growing. The sensitivity achievable with various nuclei, and thus the practical feasibility of using these nuclei in an MRI experiment, are largely governed by the concentration of the nuclear isotopes in question, their magnetogyric ratios and their nuclear spin relaxation times in the objects under study. For instance, since ^{12}C and ^{16}O isotopes are spinless, NMR studies of these very important atoms require the use of ^{13}C and ^{17}O isotopes characterized by a much lower natural abundance. This greatly complicates the MRI experiments with such nuclei, because low natural abundance leads to very low sensitivity and/or requires the use of expensive isotope-enriched samples. Nuclei with very low magnetogyric ratios are usually characterized by low sensitivity, too, and therefore are seldom used in MRI.

Nuclear spin relaxation times also determine the achievable sensitivity. Furthermore, relaxation times govern spin dynamics in MRI experiments, determine image acquisition times and are important image contrast parameters. Transverse (or spin-spin) relaxation proceeds with a characteristic relaxation time T_2 and governs the decay of an observed signal after a single radiofrequency (rf) pulse in a uniform magnetic field. In practice, the apparent signal decay rate is even faster and proceeds with a characteristic time $T_2^* < T_2$ (or $T_2^* \ll T_2$). This extra decay is caused by the differences in local magnetic fields experienced by different spins which imply different precession frequencies and gradual dephasing of the ensemble of spins in a non-uniform magnetic field. However, this extra decay caused by the distribution of local fields in the sample can be at least partially reversed by means of spin echo techniques, and thus is fundamentally different from the irreversible loss of signal characterized by T_2. After any perturbation, the system tends to return to thermal equilibrium as spins realign with respect to the static field B_0. This longitudinal (or spin-lattice) relaxation process is often exponential with a characteristic recovery time denoted as T_1.

Many imaging techniques literally scan an object to produce its image. In contrast, modern NMR and MRI techniques (as well as many other techniques such as X-ray crystallography, FT IR, *etc.*) use Fourier transform to obtain spectroscopic or spatial data. In MRI, data acquisition takes place in the space of wave vector $\mathbf{k}$ (k-space)[3–7] defined as $k_i = \gamma G_i t/2\pi$ (i = x,y,z), where G_i is the magnitude of the magnetic field gradient along coordinate i and t is the gradient duration. The original data set detected in an experiment comprises a multidimensional array of NMR

Downloaded from http://books.rsc.org/books/edited-volume/chapter-pdf/1688710/bk9781849739191-00001.pdf by guest on 03 October 2023

signal intensity values sampled for various values of **k**, achieved by varying the magnitude, the duration or the number of the applied gradients. Multidimensional Fourier transform of this data set is used to recover the true image of the same dimensionality.

As 'scanning' is done in *k*-space and not in the space of Cartesian coordinates, usually the entire data set in *k*-space has to be acquired before an image can be reconstructed. One-dimensional (1D) imaging requires an acquisition of a single line of sampled signal values in *k*-space and in principle can be performed very rapidly, within a millisecond or so. For samples which are nearly axially symmetric, acquisition of 1D axial projections can be a very efficient way to study fast dynamic processes. Higher image dimensionality usually increases the minimum imaging time substantially. The reason is that before the next line of samples in *k*-space can be acquired, one often has to wait $(3–5)T_1$ to allow the spin system to return to thermal equilibrium. As an example, for ^{1}H nuclei of water with $T_1 = 2.7$ s, a 3D image with $128\times128\times128$ volume elements (voxels) needs 128×128 lines in *k*-space to be detected, which translates into an image acquisition time of more than 36 hours $(128\times128\times3\times T_1)$. At the same time, for a sample with $T_1 = 10$ ms the same experiment can be performed in 8 min. In practice, however, the sensitivity is often an issue, and N accumulations of each line in *k*-space are performed to improve SNR in the final image by a factor of $N^{0.5}$. This makes image acquisition time N times longer and makes this approach of sensitivity improvement impractical for large values of N.

Several approaches are used to reduce imaging time in MRI. One possibility is to reduce image dimensionality. In many cases, it suffices to acquire images of a number of carefully chosen 2D slices or even 1D bars of an object. The slices to be imaged can be non-invasively selected using appropriate combinations of gradients and frequency-selective rf pulses. As a result, the observed NMR signal is produced only by the spins residing within the selected slice, eliminating the need to define the slice of interest in any destructive fashion. As most of the image acquisition time is wasted while waiting for the spin subsystem within the imaged slice to return to equilibrium, slice-selective excitation in combination with a carefully chosen interleaved acquisition of *k*-space lines for different slices allows one to acquire not just one but several 2D slices within essentially the same imaging time. Another efficient strategy widely used in MRI is the implementation of various rapid imaging techniques. One of the approaches is based on the accumulation of multiple *k*-space lines for each pulse sequence repetition. For instance, single-shot 2D imaging allows one to acquire the entire 2D image in fractions of a second, provided that the sensitivity is sufficient. Another possibility is to repeat the pulse sequence without waiting for the complete recovery of the spin system. Unfortunately, rapid imaging techniques developed and successfully used in medical MRI, work properly for bulk liquids but often fail for samples with short T_2 times such as liquids in porous media, gases and solids. At the same time, such materials are characterized by shorter T_1 times as well, sometimes allowing faster imaging using standard imaging sequences. In certain cases, T_1 times of liquids can be

Downloaded from http://books.rsc.org/books/edited-volume/chapter-pdf/1688710/bk9781849739191-00001.pdf by guest on 03 October 2023

reduced artificially by dissolving paramagnetic species, as it is done in medical MRI when paramagnetic contrast agents are administered.

For any imaging technique, an important feature is its spatial resolution. In contrast to many other techniques, however, the spatial resolution in MRI is sample-dependent. Images with the best resolution achieved to date have voxel sizes of the order of $5\times5\times5\,\mu m^3$, with some studies reporting voxels as small as $3.7\times3.3\times3.3\,\mu m^3$ or a volume of 40 femtoliters which contains 3×10^{12} proton spins of water.[8] However, the resolution of the MRI technique in many cases is limited by SNR, *i.e.*, by the sample rather than the instrument. Indeed, if the voxel size is reduced, the NMR signal intensity associated with each voxel diminishes leading to the reduced SNR in the image. Therefore, the very high spatial resolution could be obtained only using samples with large water content and many hours of imaging time.[8] In most practical applications the resolution will be (much) coarser. The resolution doesn't have to be isotropic, however, and in many cases the slice thickness can be a few mm while the in-plane resolution is from a few to a few hundred microns. The sensitivity limit on the attainable resolution means that the best applications for the MRI technique are those where the ultimate spatial resolution is not required. Higher SNR can be achieved using signal averaging, development of better hardware and more efficient pulse sequences, implementation of more sensitive signal detection methods and polarization of nuclear spins to increase the available nuclear spin magnetization. Nevertheless, one micron appears to be the ultimate limit for conventional imaging schemes which will be difficult to overcome even if a dramatic progress in sensitivity improvement can be achieved in the future. Indeed, there are other factors which limit the attainable resolution to roughly the same value of a few microns, which include diffusive displacements of molecules (especially for gases) and available magnetic field gradients (for materials characterized by short T_2 and T_2^* relaxation times).

It follows that the attainable spatial resolution may not be the strongest feature of MRI as compared to other imaging techniques. As mentioned above, the essence of MRI is the nature and flexibility of image contrast which extends well beyond the purely structural information. For instance, one might think that an n-fold increase/decrease in concentration of the detected nuclear spins should lead to an n-fold increase/decrease in the observed signal intensity. However, in many practical cases it doesn't. This is because the detected NMR signal depends not only on spin density but also on many other parameters as well. Furthermore, many essential changes in an object under study are not accompanied by a pronounced concentration change, and thus would be impossible to observe in the maps which reflect concentration only. For instance, upon freezing of water, proton spin density variation is relatively small. Nevertheless, NMR signal intensities of water and ice can differ by orders of magnitude, allowing one to detect the phase transition easily. The reason is that the NMR signal intensity can depend dramatically on molecular mobility, and this dependence provides the necessary contrast mechanism to detect the phase transition. The true

Downloaded from http://books.rsc.org/books/edited-volume/chapter-pdf/1688710/bk9781849739191-00001.pdf by guest on 03 October 2023

power of MRI is that the range of the properties and processes affecting image contrast is virtually unlimited and includes spin density, molecular mobility, diffusive and convective transport, chemical transformations, viscosity, temperature, paramagnetic additives, interactions with surfaces, electric currents, magnetic susceptibility, degree of cross-linking and ageing of polymeric materials, just to name a few. This means that, at least in principle, all these properties and processes can be studied by MRI.

This also means that the MRI measurements are *indirect*. Indeed, the only thing NMR/MRI can measure *directly* is an NMR signal and its characteristics such as magnitude, phase, resonance frequency and line width (and shape). An important feature of the MRI technique is the flexible and adjustable nature of image contrast. As a result, those sample properties which are of interest to a chemist or a chemical engineer can be made to influence the detected NMR signal. The problem is that many of sample properties usually affect the NMR signal simultaneously. Therefore, the real challenge is to single out the effect caused by a particular quantity of interest. In many cases, this is feasible but requires a lot of experience and care in the design of experiments and proper interpretation of their results.

Sometimes, the influence of object properties on the NMR signal is direct, as in the case of diffusion or flow of fluids in a magnetic field gradient which directly affect signal intensity or phase, respectively. In many cases, however, this influence is imposed *via* certain mediators. For instance, in the example with water and ice considered above, the mobility of molecules affects nuclear spin relaxation times (T_1, T_2), which in their turn affect the NMR signal. Relaxation times of nuclear spins are directly related to molecular mobility and therefore can provide useful information on the frequency spectrum of molecular motions, their activation energies and correlation times, and distances at the molecular scale. Apart from relaxation times, there are other characteristics of a spin system which can act as mediators, for instance chemical shift (or local magnetic fields in general), spin polarization, spin–spin interactions, *etc.* All this makes it possible to tailor an MRI experiment to the needs of a particular study and to extract useful and diverse information about objects and processes. It is worth mentioning that while appropriately weighted images usually give qualitative information only, one can also obtain quantitative maps of various parameters by evaluating the parameter of interest for each image voxel. This allows one to obtain maps of local velocities, diffusivities, temperatures, chemical composition and so on.

3 Practical aspects and structure visualization

NMR instruments with 200–500 MHz ^{1}H NMR frequency equipped with (micro)imaging accessories provide high sensitivity and high spatial and spectroscopic resolution. In addition, they are normally equipped with a vertical bore superconducting magnet, which is most suitable for the studies of certain reactor types such as trickle bed and fluidized bed reactors. The geometry of the magnet and the rf probe limits the

Downloaded from http://books.rsc.org/books/edited-volume/chapter-pdf/1688710/bk9781849739191-00001.pdf by guest on 03 October 2023

maximum reactor diameter to a few cm which has to fit into the rf coil/gradient coils assembly. While the reactor and catalyst bed lengths are essentially unlimited, the axial dimension of the sensitive region is also limited to a few cm. These size restrictions combined with the limitations on the materials that can be present in the magnet/probe assembly during an NMR/MRI experiment (see below) require the construction of an MRI-compatible model reactor. NMR/MRI instruments equipped with horizontal bore magnets often have wider bores, but cannot accommodate long vertical reactors and thus require different reactor designs. Sensitivity and/or spatial resolution in the detected images decreases significantly for rf probes with larger volumes, therefore some compromise is necessary.

In high resolution NMR of liquids, higher magnetic fields (600–1000 MHz ^{1}H NMR frequency) provide even higher spectral resolution and SNR. However, for heterogeneous objects, higher applied magnetic fields lead to larger local magnetic field gradients within the sample and may cause various image artifacts and significant loss in SNR. Systems with low magnetic fields (<200 MHz) can accommodate larger reactors, but such experiments usually suffer from reduced sensitivity and thus lower absolute spatial and temporal resolution. Nevertheless, one of the recent trends in the applications of NMR and MRI in materials science and chemical engineering is the design and construction of instruments that use low and ultra-low magnetic fields.[9–12] In addition to lowering the costs, this allows one to remove some of the restrictions associated with the use of high-field systems, and in particular to take an instrument out of the rigorously controlled environment of a scientific NMR/MRI laboratory and bring it to a chemistry lab or even to an industrial site. Furthermore, some have an open design and thus eliminate the need to place an object under study inside a restricted space of a probe. The necessary prerequisite for many such applications is a significant boost in detection sensitivity of NMR/MRI, which happens to be another hot topic in modern magnetic resonance. While the utility of low-field MRI is still to be demonstrated for catalytic applications, an increased SNR is also very useful for high-field studies, and recent examples of such applications are discussed below.

In addition to size restrictions, many conventional reactor designs are not suitable for MRI studies for a number of other reasons. It is therefore necessary to construct a model reactor compatible with an MRI instrument. For MRI studies of a reactor (*e.g.*, packed catalyst bed) structure, various transport processes and those catalytic reactions that can be carried out at ambient temperature and pressure, a piece of glass or plastic tubing will work as the main construction element of the reactor, even though plastic materials may contribute to the detected image (*e.g.*, ^{1}H MRI). However, the most interesting and also challenging applications require substantially elevated pressures and temperatures within an operating reactor, especially when dealing with highly exothermic reactions. This poses certain problems, as the expensive MRI hardware has to be protected from high temperatures as well as from accidental damage associated with high pressures inside the vessel residing inside

Downloaded from http://books.rsc.org/books/edited-volume/chapter-pdf/1688710/bk9781849739191-00001.pdf by guest on 03 October 2023

the magnet/probe assembly. At the same time the most obvious choice of construction materials, *viz.* metals, is generally not an option. Electrically conducting containers, including non-magnetic metals, cannot be used for constructing MRI-compatible reactors as they are impermeable to rf electromagnetic fields that are used in NMR/MRI for signal transmission and reception. Bulk metallic parts should be avoided also because pulsed magnetic field gradients used in MRI induce eddy currents in electrically conducting materials. For studies at ambient pressures or slightly above, thick-walled temperature-resistant glass or quartz can be used. For instance, in the design reported in ref. 13 exothermic reactions were safely performed at temperatures around or slightly above 100 °C (catalyst temperatures up to 250 °C during exothermic hydrogenation reactions) with the use of an evacuated double-walled glass Dewar. Essentially, the reactor comprised three concentric glass tubes. The catalyst was placed inside the inner tube (10 mm i.d.). The annular space between the inner and the middle tubes was used to heat the catalyst with a stream of air preheated to 80–100 °C. The entire reactor was inserted into the rf coil/gradient coils assembly located in the vertical bore of the NMR magnet (300 MHz, Avance DRX 300 NMR spectrometer, Bruker). The gradient coils of the instrument can be damaged if heated above 60 °C. To prevent this, the middle and the outer tube of the reactor and the annular space between them formed a vacuumed Dewar. Alternatively, an active heating/cooling with a liquid can be implemented. For instance, a fluorinated liquid hydrocarbon will allow one to avoid a strong background ^{1}H NMR signal.[14] However, the passive heat protection of the design reported in ref. 13 avoids heat removal from the reaction zone. The inner tube accommodated the catalyst and also served as a duct for supplying gaseous reactants, while liquid reactant, if required, was supplied to the catalyst through an additional capillary. In the experiments performed with a single catalyst pellet, the latter was suspended on a thermocouple implanted into the cylindrical pellet though its side. In the experiments with a catalyst bed, the latter rested on a stainless steel mesh. Pulsed magnetic field gradients used in MRI induce eddy currents in electrically conducting materials and can severely distort or even destroy the image. Therefore, the mesh was located well outside the sensitive region of the rf probe. The thermocouple was only 0.2 mm in diameter, but nevertheless it destroyed the signal in its immediate vicinity, and in addition worked as a pick-up antenna which fed extra noise and interferences from outside the magnet directly into the rf coil. The reactor design[13] ensured that the temperature at the outer wall of the reactor never exceeded 50 °C. The entire reactor was *ca.* 25 mm in diameter and thus could be inserted in a 25 mm i.d. birdcage rf insert (Bruker), but the probe body had to be redesigned to have a 25 mm bore through the entire probe. The reactor in ref. 14 was used at temperatures up to 125 °C and pressures of 10 bar but under non-reactive conditions. Recently, MRI experiments were reported that used a reactor capable of withstanding temperatures of *ca.* 300 °C and pressures of *ca.* 30 atm, with the reactor units made of Si_3N_4.[15] This brings the MRI studies one step closer to practically relevant conditions of reactor operation.

Downloaded from http://books.rsc.org/books/edited-volume/chapter-pdf/1688710/bk9781849739191-00001.pdf by guest on 03 October 2023

Knowing the internal structure of a reactor (*e.g.*, a packed catalyst bed) is important as it can have important influence on the heat and mass transport processes within the operating reactor and the overall reactor efficiency. MRI can be used to visualize the internal structure of a model reactor in a non-invasive manner, even for optically opaque materials as long as they are NMR/MRI-compatible (see above). Structure visualization of a multi-phase system can be done in several different ways. MRI is best performed using an NMR signal of a liquid phase. Therefore, the most straightforward way of visualizing a structure of, *e.g.*, a bed of solid elements is to completely flood it with a suitable liquid (water, organics) and acquire an image of the liquid phase.[6,14,16–22] The voids of the bed will thus be visible in the image directly as they will give a strong signal, whereas solid phase will be imaged indirectly as areas that give no observable signal (Fig. 2a). For porous solids, the image resolution (tens to hundreds of microns) is usually much coarser than the sizes of individual pores. This means that image pixels corresponding to liquid in the inner regions of porous solids would give a signal with intensity lower than the bulk liquid because of the porosity value being less than unity, and thus can be distinguished from both liquid-filled voids (maximum signal intensity) and bulk solid phase (no signal) in beds comprised of porous particles. In addition, the signal of an intrapore liquid is often additionally reduced because of its reduced nuclear spin relaxation times. This latter fact can be employed to manipulate image contrast because relaxation effects are sensitive to the parameters of an imaging pulse sequence used, providing a researcher with additional means of revealing the structure of an object (reactor) under study.

Another possibility to image a structure consisting of porous solid elements and voids is to saturate the porous material with a suitable

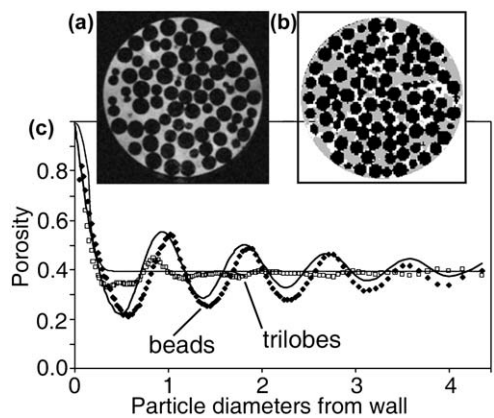

Fig. 2 (a) 2D image of a bed of glass beads 2 mm in diameter saturated with a liquid (solid phase is shown in black, liquid phase in grey). (b) An image detected during the two-phase gas-liquid flow in the bed (solid phase is shown in black, liquid phase in white, and gas phase in grey). (c) Radial distributions of porosity for beds of spherical glass beads and Al_2O_3 trilobes (diameter 1.3 mm, length 4 mm) extracted from the images of the liquid-flooded beds. Solid lines show the results of model calculations. Reproduced from ref. 17 with permission of Wiley-VCH Verlag GmbH & Co. KGaA, Weinheim.

Downloaded from http://books.rsc.org/books/edited-volume/chapter-pdf/1688710/bk9781849739191-00001.pdf by guest on 03 October 2023

liquid. In this case, the liquid-containing phase can be imaged directly (high signal intensity in an image) while liquid-free voids will appear in the image as areas void of any signal. As bulk liquid is not present in such an experiment, the SNR will be lower and acquisition times longer as compared to the experiment with the liquid-flooded reactor. A variant of these two strategies is to use a gas instead of a liquid. If the gas used is not adsorbed in the pores of a solid phase, the image contrast will be similar to that obtained for a liquid-flooded reactor, but SNR will be significantly lower because of a much lower spin density of gases compared to liquids. On the other hand, if gas adsorbs strongly in the pores of a solid phase, the latter may appear in the image as hyperintense areas as compared to gas-filled voids.

Yet another possibility is to image the solid phase directly. Usually, imaging of solid materials is much more difficult as compared to liquids because of very short transverse relaxation times and significant broadening of the signals in NMR spectra of solid materials. Therefore, imaging of solids is often performed with the use of specialized MRI hardware and pulse sequences.[4,23–28] However, because line broadening in solid samples is often inhomogeneous, certain solids can be addressed using simple imaging strategies such as the spin echo method.[29–37] In particular, the ^{27}Al nucleus can be used for direct imaging of aluminium-containing materials[29–31,33,34,38] such as γ-Al_2O_3, glass, refractory cement/concrete, *etc.* Considering that γ-Al_2O_3 is often used as catalyst support, this provides some interesting possibilities to use ^{27}Al MRI, including the ^{27}Al NMR/MRI thermometry considered in more detail in the corresponding section below. At the same time, direct imaging of solids is usually time-consuming because of the unfavorably low signal intensity in most studies.

Once the packed bed structure is imaged, the data can be processed to extract essential information such as distribution of pore (void) sizes, connectivity, radial porosity distribution (Fig. 2c), *etc.*[14,17–22] In addition, the known structure of a packed bed can be used as a direct input in model calculations of transport and reaction within it.[21,22,39] Knowing the partitioning of the structure into solid phase and interparticle voids is also essential when studying processes in three-phase systems such as gas-liquid-solid reactions. In most cases, the gas is not (or cannot be) observed in the images of a liquid-containing reactor. However, if the geometry of the void space is already known, then that part of void space which does not contain liquid (*i.e.*, does not give a strong signal associated with a liquid) obviously carries the gas phase (Fig. 2b).[6,7,14] Sometimes, both the liquid and the gas phases in the bed voids can be visualized directly, for instance using ^{1}H MRI of a liquid (*e.g.*, water) and ^{19}F MRI of a gas (*e.g.*, SF_6).

In certain cases, reactors may have a dynamic 'structure'. An example is a bed of solid particles fluidized with a gas flowing through it. At present, MRI is too slow to map the instantaneous positions of the solid phase in a fluidized bed of solid particles. At the same time, the technique is suitable for visualizing the time-averaged structure of a fluidized bed. In most cases, liquid-containing solid particles (oil-containing seeds,

Downloaded from http://books.rsc.org/books/edited-volume/chapter-pdf/1688710/bk9781849739191-00001.pdf by guest on 03 October 2023

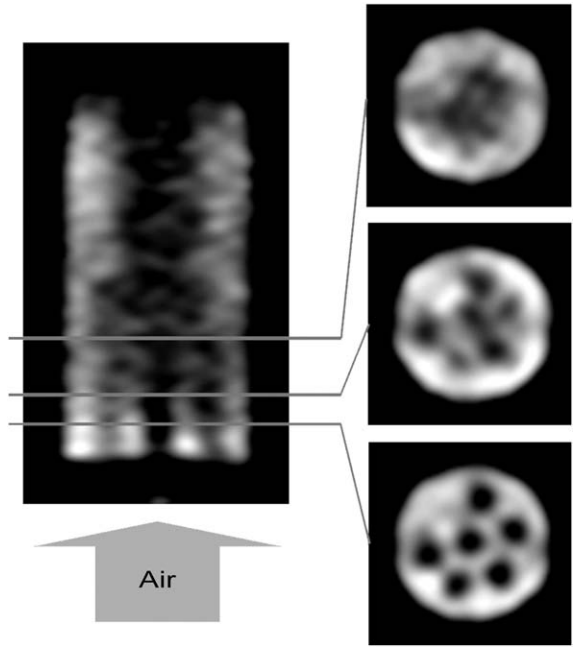

Fig. 3 ^{27}Al MR images of a fluidized bed of alumina powder in a vertical cylinder. Air is supplied through the orifices at the bottom (one orifice got plugged). One vertical (left) and three horizontal 2D slices (right) of the full 3D data set are shown. Lighter shades correspond to higher signal intensities, *i.e.*, to higher time-averaged concentrations of the solid phase.

porous grains saturated with non-volatile liquids, *etc.*) are used for this purpose to get the highest possible NMR signal.[40–42] At the same time, γ-Al_2O_3 powder used as the solid phase can be imaged directly using ^{27}Al MRI (Fig. 3). Usually, the images show the density of the fluidized phase averaged over the image acquisition time, with the signal intensity in the images proportional to the average concentration of the solid phase. Such images can reveal spatial structure of gas jets and can provide time-averaged flow velocities. Dynamic events such as bubbling can be addressed using 1D imaging or fast 2D imaging schemes.[40]

4 Mass transport in channels, voids, and porous materials

NMR has a long and successful history of application for the studies of molecular diffusion of liquids and solutes. Pulsed field gradient (PFG) NMR experiment is based on the application of a pair of gradient pulses, which lead to the NMR signal reduction for stochastically moving molecules.[3,5,43] Analysis of the results of such an experiment can yield effective (but possibly time scale dependent) diffusivity value or even the complete diffusion tensor. PFG NMR is extensively used to study diffusion in various systems including porous solid materials of relevance to catalytsis.[42–53] Such studies are often performed without the imaging capabilities (*i.e.*, without spatial resolution).

Downloaded from http://books.rsc.org/books/edited-volume/chapter-pdf/1688710/bk9781849739191-00001.pdf by guest on 03 October 2023

Mass transport involving liquids, and to a lesser extent – gases and granular solids, can be also addressed with MRI using two general approaches.[43,54] The first approach is based on creating an initial gradient of a tracer substance and then using MRI to repeatedly map the evolution of tracer concentration in space and time. If a tracer gives a detectable NMR signal which changes as the local tracer concentration is changed, it can be imaged directly. For instance, transport of fluids in porous materials during drying and sorption processes is sometimes used as a model of transport in porous media and can be studied by detecting the images of the fluid in the porous space of a sample and analyzing their changes in time.[54] Certain tracers that do not give an observable signal can provide negative contrast, for instance when diffusion of a deuterated liquid into a sample saturated with its protonated analog is monitored using ^{1}H MRI (H_2O/D_2O exchange). Transport of some NMR-silent tracers can nevertheless produce observable changes in the images as well. For instance, paramagnetic ions reduce nuclear spin relaxation times of a solvent, and thus their transport can be tracked by detecting the relaxation-weighted images of the solvent. Clearly, the mass transport distances addressed by all such experiments cannot be smaller than the spatial resolution of the detected images.

There is an entirely different possibility provided by NMR/MRI which can be used to study transport even in the absence of any tracer gradients. Furthermore, it essentially does not require an introduction of any tracers in a system under study. It is based on tracking the displacement of molecules of the fluid phase which is already present in the object under study, *i.e.*, uses nuclear spins of the fluid molecules as 'tracers' and manipulates those spins to detect fluid transport. Depending on the character of transport, the length scale and the information required, the MRI toolkit provides several different instruments to address the problem. The spatial tagging method essentially draws ''tags'' on the image of a sample under study, and after a certain delay visualizes their transformation caused by fluid transport.[7,43,55–57] The tags are non-invasive; they are produced by manipulating nuclear spin magnetization of the fluid molecules and appear as contrast stripes in the images. The molecules carry this altered magnetization as they are transported by the fluid flow, making the original tags to transform accordingly. The method is usually applicable to transport in relatively large channels. The time-of-flight is another method[43,55,57] based on disturbance of the NMR signal in a particular region of the sample by the rf pulses, but involves observation of subsequent changes in the signal intensities of the pixels of an MR image caused by the displacements of the perturbed and unperturbed spins in the sample, providing qualitative or semi-quantitative information on transport.

Quantification of velocities and mapping the velocity fields of flowing fluids are often carried out using the phase method.[3,7,43,55–59] The corresponding pulse sequence is designed to make the phase of the acquired signal proportional to the fluid flow velocity. As the phase of an NMR signal depends on many things, usually two measurements are required to extract the contribution to the signal phase caused by flow.

Downloaded from http://books.rsc.org/books/edited-volume/chapter-pdf/1688710/bk9781849739191-00001.pdf by guest on 03 October 2023

Measurements with and without flow can be used if the latter can be stopped; alternatively, measurements with and without flow-encoding magnetic field gradients can be implemented. Once the phase change associated with flow is extracted, it can be used to quantify flow velocity. Strictly speaking, the method measures the displacement of fluid during the time interval between two gradient pulses. Therefore, if velocity is not constant in time, the obtained effective velocity will depend on the time interval of the measurement. In addition, if different regions of the fluid travel at different velocities, a single value of effective velocity will be measured that in general does not correspond to the true average velocity. When the phase method is combined with MRI, it will yield the spatial velocity map showing effective velocities for each image pixel (voxel). The technique is applicable to the studies of flow in macroscopic channels and in some porous materials such as packed beds if the spatial resolution is sufficient to clearly resolve the transport channels. If the characteristic pore sizes are much smaller than the spatial resolution achieved, only effective velocities for a large number of pores covered by image pixel (voxel) can be evaluated. Transport of liquids and gases can be addressed, with gases showing lower SNR because of a much lower density. At the same time, the successful attempts to perform gas flow imaging show that large diffusive displacements of molecules do not prevent one from addressing convective displacements with MRI. This is because chaotic fluid displacements lead to signal attenuation but do not affect its phase. Therefore, even in the presence of relatively large diffusive displacements, smaller convective displacements can be evaluated from the signal phase if SNR is sufficient. Signal reduction caused by chaotic motion also makes unsteady, transient and turbulent flows much more difficult to address. Nevertheless, implementation of faster and more robust pulse sequences makes it possible to successfully address turbulent and unsteady flows. Velocities from a few μm/s up to ~10 m/s can be addressed using phase method.

In certain cases, the information on the distribution of flow velocities or diffusive or dispersive displacements in a sample (a histogram of velocities or displacements) may be more relevant than the spatial assignment of average transport velocities (flow velocity map). The tool for this is based on the measurement of the average propagator of motion, $P(R,\Delta)$, which gives the relative quantity of the fluid that traveled over distance R in time Δ.[3,7,43,55,58,59] The displacements R are along the direction of the applied gradients, and Δ is the separation of the gradient pair, so both the direction and the time scale can be varied, if necessary. The propagator $P(R,\Delta)$ reflects all displacements of the fluid independent of their nature. If diffusive displacements dominate and are isotropic, $P(R,\Delta)$ will have a Gaussian shape, will be centered at $R = 0$ and will get broader for larger time scales (larger Δ). If convection dominates, $P(R,\Delta)$ will be shifted away from the origin and will reflect distribution of flow velocities and flow dispersion effects in the direction of the applied gradient. Many such studies of diffusion, flow, filtration and other transport processes are performed without spatial resolution, *i.e.*, for the entire sample or some part of it. The corresponding experiments are

Downloaded from http://books.rsc.org/books/edited-volume/chapter-pdf/1688710/bk9781849739191-00001.pdf by guest on 03 October 2023

often considered as imaging in the space of molecular displacements ('*q*-space imaging') in contrast to the conventional MRI performed in the space of position coordinates ('*k*-space imaging'). Furthermore, measurements of the average propagator may be combined with an MRI experiment. This will provide spatially localized distributions of displacements for each pixel (voxel) of the image; however, such experiment will be significantly more time-consuming. There are more sophisticated tools in the MRI toolkit; they allow one to measure acceleration rather than velocity, to correlate diffusive or convective displacements at two different time instants, *etc.*[58,60–65] All these methods, however, usually require a prolonged signal accumulation and may still suffer from low SNR and low spatial resolution.

Applications of MRI to transport studies in model reactors and other geometries were extensively reviewed in the literature.[7,42,43,56,66–68] In particular, distribution of liquid phase in a packed bed during gas-liquid two-phase flow in the absence of any reaction was mapped at ambient conditions[7,42,43,56] or at elevated temperatures and pressures (see Fig. 2b).[14,17] Through the detection of liquid phase distribution it was demonstrated that local liquid pulsing events can promote transition from trickle to pulsing flow regime.[7,42] Detection of the images of the liquid phase was also used to address bubble-train and film flow in the channels of ceramic monoliths.[7,69] Phase method was applied to obtain velocity maps for single-phase flow of liquids or gases in packed beds,[7,18–20,70–72] porous ceramic materials,[73] monoliths,[70,74–77] model string-type reactor (Fig. 4a),[78] diesel particulate filters.[79,80] In addition, for the two-phase gas-liquid flow in a packed bed of glass beads, the velocity maps of both the gas and the liquid phase in the bed were acquired[42,67,81] (Fig. 4b). The flow imaging times amounted to tens of minutes for both liquid (water, ^{1}H MRI,) and gas (SF_6, ^{19}F MRI), and the

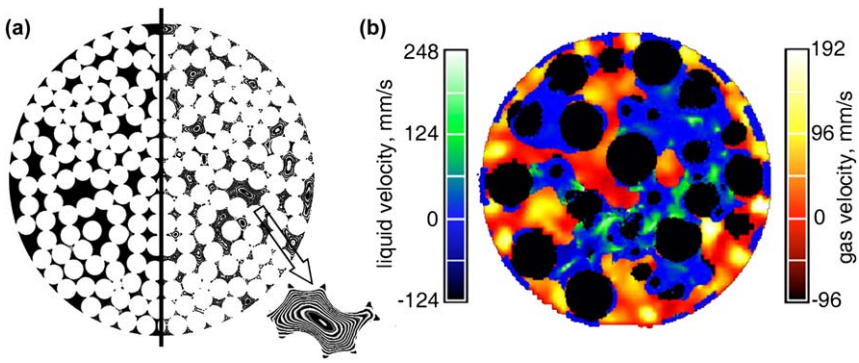

Fig. 4 (a) A 2D image (left half) and water flow velocity map (right half) of a model string-type reactor comprising a bundle of non-porous plastic rods 1 mm in diameter packed in a cylinder. The solid phase is shown in white. The flow map is a contour map showing isolines of the axial flow velocity; it is reflected horizontally so that both parts of the figure correspond to the same half of the reactor cross-section. (b) Flow velocity maps of gas (SF_6; red/yellow) and liquid (water; blue/green) flowing down co-currently in a packed bed of 5 mm glass beads. Color is available in the electronic version of this figure. Fig. 4 (b) is reproduced from ref. 81 with permission of Elsevier BV.

Downloaded from http://books.rsc.org/books/edited-volume/chapter-pdf/1688710/bk9781849739191-00001.pdf by guest on 03 October 2023

in-plane spatial resolution in water images/maps (177 μm) was significantly better than for the gas phase (708 μm). The average propagator method was applied to obtain the distribution of velocities in numerous studies of flow and dispersion of liquids in porous media, including packed beds,[58,60,70–73,77,82–87] and was also extended to flow and filtration of gases in various geometries[60,68,70,74–76,88–90] and gravity-driven transport of fine alumina powder through a packed bed of alumina beads.[60,91]

One of the recent trends is an attempt to significantly reduce flow imaging times in order to approach snapshot MRI velocimetry of unsteady-state processes. Comparison of the performance of different imaging sequences in this context is summarized in ref. 67. In single-phase flow, significant interest focuses on unsteady-state flows and the transition to turbulence. For instance, sequences based on echo-planar imaging (EPI) method were used to address turbulent flow and laminar-turbulent flow transition for single-phase liquid flow in a pipe,[67,92] with the maps of all three velocity components detected in 60 ms.[67] The fastest approach appears to be the one based on spiral imaging method which uses data sampling along a spiral trajectory in the *k*-space. In particular, spiral imaging was used to address pipe flow at Re = 4500, providing 91 images acquired per second with an in-plane spatial resolution of 625 μm × 625 μm.[93] Spiral flow imaging was also demonstrated for gas-liquid bubbly flow, and in particular to monitor a single rising bubble and to measure the vertical velocity component of the liquid around it.[67] Further reduction in flow imaging time was achieved based on the implementation of compressed sensing schemes which allow one to strongly undersample the signal in the *k*-space without the penalty of a significantly compromised data quality.[94] Sampling of only 33% of the number of data points in *k*-space provided flow maps for SF_6 in a bed of spheres of essentially the same quality and at the same spatial resolution as compared to the acquisition of the conventionally acquired full set of *k*-space data points.[67] This approach was used to acquire velocity maps in 3 ms and monitor dynamic transport events at the rate of 188 velocity maps per second for flow mapping of a single bubble rising in a liquid to study its wobbling motion and observe vortex shedding in its wake.

Many other transport processes relevant to chemical engineering and catalysis have been addressed. In particular, MRI was successfully used to monitor the process of preparation of supported catalysts by impregnation from solution of an active component precursor. The properties of the final catalyst, including the macroscopic distribution of an active component within the support pellet, depend critically on the mass transport processes in the course of impregnation, which in turn depend on numerous factors such as solution composition, impregnation conditions, interaction of solutes with each other and with the support surface, *etc.* In this context, direct imaging of the transport is possible for only a limited number of chemicals that give a strong NMR signal. For instance, ^{31}P MRI was used to visualize the transport of $H_xPO_4^{(3-x)-}$ into a γ-Al_2O_3 pellet after it was immersed in an aqueous solution of H_3PO_4.[16,37,95–98] Transport of $H_xPO_4^{(3-x)-}$ into the pellet was shown to be slow even under conditions of a fast capillary imbibition of water into the

Downloaded from http://books.rsc.org/books/edited-volume/chapter-pdf/1688710/bk9781849739191-00001.pdf by guest on 03 October 2023

dry pellet. The images detected during impregnation were also compared with the ^{31}P images detected after terminating the impregnation at various stages and drying the pellet,[36,95] showing that the distributions of phosphate in the liquid phase during impregnation and of the adsorbed phosphate were quite similar. The same direct approach was used to study the transport of ^{13}C-labeled citric acid in an alumina pellet at different solution pH values using ^{13}C NMR signal detection.[99] Another illustrative example is the direct detection of the ^{195}Pt NMR signal to image the impregnation of a γ-Al_2O_3 pellet with an aqueous solution of H_2PtCl_6, albeit the concentration had to be high to ensure acceptable SNR.[95]

Another demonstrated approach is indirect in the sense that the distribution of a certain chemical is mapped by detecting the NMR signal of the intrapore liquid. Nuclear spin relaxation times of the latter can change significantly in the presence of certain molecular species either dissolved in the liquid filling the pores or adsorbed or precipitated on the pore walls. In such cases, the relaxation-weighted image of the solvent (*e.g.*, ^1H MRI) in the pores of the support will reflect local concentrations of a solute or adsorbate. This approach is advantageous since high concentration of the solvent often gives the highest SNR. In particular, many supported catalysts are prepared using solutions containing complexes of paramagnetic metal ions such as Co^{2+}, Ni^{2+}, Cu^{2+} or Fe^{3+} which significantly reduce nuclear spin relaxation times of liquids. Transport of Co^{2+} aqua complexes ($[Co(H_2O)_6]^{2+}$) during the incipient wetness impregnation of individual cylindrical γ-Al_2O_3 pellets was addressed with this approach.[16,37,98,100] Repeated detection of relaxation-weighted 2D images of water in the pellet during the impregnation process visualized the transport of $[Co(H_2O)_6]^{2+}$. Using an independent calibration experiment, the images were then converted into quantitative maps of Co^{2+} concentration in the pellet at different stages of impregnation. Such experiments performed under various conditions (solution pH, various concentrations of additives, *etc.*) revealed differences in the spatial distribution of Co^{2+} (egg-yolk, egg-white, egg-shell or uniform) in the support.[101] Similar studies were performed to visualize the transport and quantify distribution of Ni^{2+} [102] and Cu^{2+} [99] complexes in γ-Al_2O_3 pellets upon their impregnation with aqueous solution of corresponding salts. Redistribution of an active component during the drying stage can be also addressed. In this case, after removing water from the pellets they were saturated with cyclohexane[99,103] which is not expected to alter the distribution achieved in the drying stage but which gives suitable NMR signal sensitive to the presence of paramagnetic species on the pore walls of the support.

Furthermore, it was also established that some diamagnetic solutes and/or adsorbates can change the relaxation times of liquids in the pores of a support as well (Fig. 5).[104] This fact was used to study the dynamics of $PtCl_6^{2-}$ transport in a support pellet immersed in an aqueous solution of H_2PtCl_6 and oxalic acid, with the ^1H NMR signal of water used to detect the image. Similar studies were performed with $PdCl_4^{2-}$ in alumina pellets, and also to study the distribution of Pt and Pd in honeycomb monoliths.[105] Similarly, differences in the relaxation times of n-heptane

Downloaded from http://books.rsc.org/books/edited-volume/chapter-pdf/1688710/bk9781849739191-00001.pdf by guest on 03 October 2023

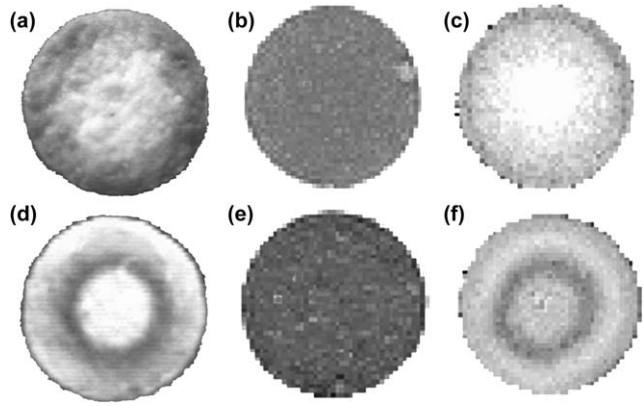

Fig. 5 Alumina pellets with an egg-shell (a–c) and egg-white (d–f) distribution of $PtCl_6^{2-}$. Digital camera images (a,d) were obtained after the pellets were cut and treated with a $SnCl_2$ solution; darker shades correspond to higher Pt contents. Proton spin density (b,e) and T_1 (c,f) maps of cyclohexane were constructed from the MR images obtained after dry pellets were saturated with cyclohexane; darker shades in (c,f) correspond to longer cyclohexane T_1 times.

in Pd/Al_2O_3 and Al_2O_3 particles were used to distinguish the catalyst and support particles in a bed comprising their random mixture.[106] The relaxation contrast approach was also used to study transport of $Mo_7O_{24}^{6-}$ ions in γ-Al_2O_3 pellet during its impregnation with an aqueous solution of $(NH_4)_6Mo_7O_{24}$ [37,98,99] and to map the distribution of Mo after pellet drying.

An approach similar to the one described above can be used to study distribution of carbonaceous deposits in a catalyst upon its deactivation, since formation of weakly paramagnetic deposits in a porous catalyst reduces relaxation times of the intrapore fluids and blocks pore space which leads to a reduced NMR signal intensity. These facts were used to visualize macroscopic distribution of coke in cylindrical alumina pellets after their 50–100% deactivation in ethanol dehydration to ethylene by saturating the pellets with water before imaging.[107] Similar studies were performed with HY zeolite pellets partially coked in n-heptane cracking, with 2,3-dimethylpentane used as a probe molecule for MRI.[108,109] In all these studies, distribution of coke in the catalyst pellets was found to be non-uniform. Direct imaging of coke using its ^1H NMR signal was also successfully demonstrated in the study that addressed HZSM-5 catalyst pellets prepared with binder and coked in methanol-to-gasoline conversion to 20.5 wt% coke content.[110] Such study requires the application of specialized MRI techniques because the detected signals have very short T_2 times. In the same study, an alternative indirect approach was demonstrated based on significant differences in the T_1 times of propane in the coked and uncoked catalyst. Images of coke distribution were also obtained for naphtha reforming catalyst ($Pt\text{-}Re/Al_2O_3$) and alumina pellets using T_1 maps of adsorbed n-heptane.[111] The experiments revealed the presence and non-uniform removal of residual coke after the catalyst regeneration at different temperatures.

Downloaded from http://books.rsc.org/books/edited-volume/chapter-pdf/1688710/bk9781849739191-00001.pdf by guest on 03 October 2023

5 Operando studies of model reactors

5.1 Distribution and transport of liquids and gases

As discussed in the preceding section, mass transport processes in model reactors are often studied under non-reactive conditions, for instance with the use of plastic or glass beads instead of the actual catalytic solids, and with water/air supplied instead of the actual reactants. While this approach may be useful to address some general features of mass transport processes in model packed beds, the observed picture may be very different under reactive conditions. In particular, in trickle bed reactors the distribution of the liquid phase in the void space and in the pores of catalyst particles may change drastically once, *e.g.*, an exothermic reaction is turned on. This happens because in an operating reactor the mass and heat transport processes may be essentially coupled to each other and to the catalytic conversion, exhibiting highly non-linear behavior even under steady-state conditions, and in addition may lead to complex dynamic behavior of an operating reactor. Therefore, it is not surprising that currently there is a significant interest in the development and application of various spectroscopic and imaging techniques for the *in situ* and operando studies of operating catalytic reactors.[112–115]

The dramatic difference between the distribution of a liquid phase in a fixed catalyst bed with a cocurrent gas-liquid flow under reactive and non-reactive conditions was demonstrated by MRI using heterogeneous catalytic hydrogenation of 1-octene as a model process (Fig. 6).[116] The reaction could be turned off by switching from H_2 to N_2 in the gas feed while keeping the flow of liquid 1-octene unchanged. The 2D images of the liquid phase distribution were detected and processed to yield the 2D maps of the spatial distribution of the external and internal liquid holdups for various regimes of the reactor operation. The results revealed that under reactive conditions the distribution of the liquid phase in the catalyst bed was highly non-uniform. In contrast, in the absence of reaction, the bed was largely filled with the liquid phase. Even though the reaction conditions were far from those used in practice, the difference in behavior with a non-reacting system was quite dramatic.

One of the interesting and useful models of an operating system is a single-catalyst-pellet reactor. While it may not exhibit the behavioral complexity of an operating packed bed, it is still a viable model for many dynamic processes that may take place on the length scale of a single catalyst pellet and thus may provide an insight into the appearance of critical phenomena and their expansion to a larger scale. In the very first MRI studies of gas-liquid-solid catalytic processes,[16,28,32,60,70,98,117–120] heterogeneous catalytic hydrogenation of α-methylstyrene (AMS) was chosen as a suitable model process. The experiments imaged the spatial distribution of liquid phase in the catalyst pellet during the reaction, without discriminating the contributions of AMS and the hydrogenation product cumene. To mimic various experimental conditions, AMS was supplied to a cylindrical Pt/γ-Al_2O_3 pellet either as a liquid (through a capillary to the top surface of the pellet), or as a vapor (by bubbling the supplied H_2 through liquid AMS), or both. The results clearly

Downloaded from http://books.rsc.org/books/edited-volume/chapter-pdf/1688710/bk9781849739191-00001.pdf by guest on 03 October 2023

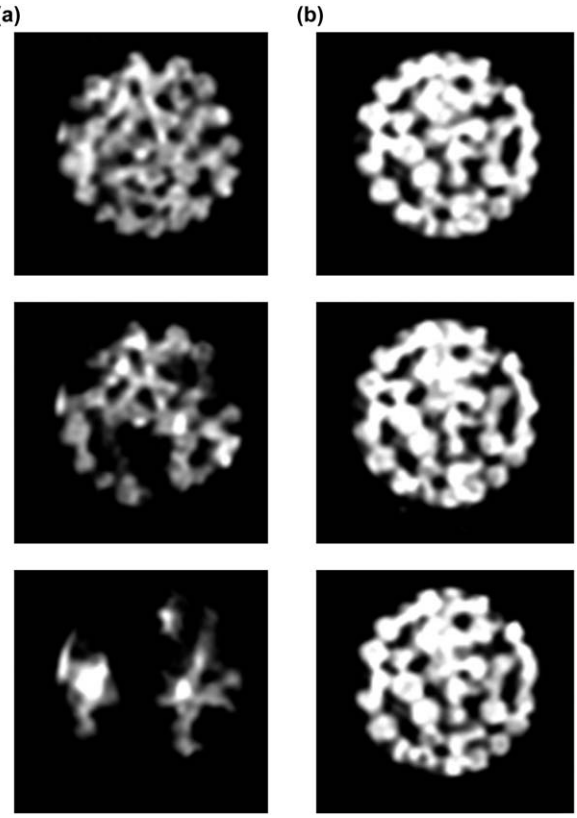

Fig. 6 ^{1}H MR images showing the distribution of the liquid phase in the catalyst bed under reactive conditions (a) and without reaction (b). Liquid 1-octene was supplied at different flow rates along with H_2 (a) or N_2 (b) to the bed of 1% Pd/γ-Al_2O_3 catalyst beads 3.2 mm in diameter.

demonstrated that even if AMS was supplied only as a vapor, some amount of liquid could be seen in the pores of the catalyst owing to AMS and/or cumene vapor adsorption or condensation. When liquid AMS supply to the top edge of the pellet *via* a capillary was turned on, the upper part of the pellet was observed to contain substantially more liquid than its lower part. Essentially, the upper part provides a substantial reservoir of the liquid reactant available for evaporation, while the lower dry part is able to efficiently perform gas-phase hydrogenation of AMS vapor, with short distances between the evaporation and reaction zones that AMS vapor has to travel to enter the active zone. The catalyst pellet temperature increased significantly once the liquid AMS supply was turned on, confirming the efficient progress of the reaction. At higher flow rates of liquid AMS, the pellet was filled with the liquid phase progressively until it was completely flooded, which leads to a significant reduction of the reaction rate as it becomes limited by the diffusion of H_2 through the liquid phase to the active catalytic centers. These results confirmed the existence of the high- and low-temperature steady states for the operating catalyst. In the experiments performed without AMS

Downloaded from http://books.rsc.org/books/edited-volume/chapter-pdf/1688710/bk9781849739191-00001.pdf by guest on 03 October 2023

vapor supply,[60,70,117,118,120] different initial pellet conditions and variation of the liquid AMS flow rate were used to monitor the distribution of the liquid phase in the pellet on the upper and lower branches of the temperature hysteresis curve as well as during the transition periods.

The 2D images in the early studies discussed above were acquired in *ca.* 260 s using the conventional spin echo pulse sequence. Subsequent experiments were carried out with grains of the 1 mass% Pd/γ-Al_2O_3 catalyst containing 0.1 mass% Mn[13,32,35,120–122] since paramagnetic ions reduce the T_1 time of the pore liquid and proportionally reduce the image acquisition time. This made it possible to acquire two-dimensional images in 34 s and thus to visualize a number of interesting dynamic processes in the operating single-pellet reactor, including the dynamics of liquid phase redistribution within the pellet during single and multiple catalyst ignition events, oscillations of the liquid content and a reciprocating motion of the liquid front in the catalyst pellet (Fig. 7).[13,32,121] The results obtained demonstrate the ability of MRI to visualize complex dynamic behavior of an operating single-pellet catalytic reactor resulting from a non-linear coupling of the transport processes involved with the exothermic hydrogenation of an unsaturated compound. Mathematical modeling of the experimental results[123] allowed the authors to confirm that the oscillations in temperature and liquid content distribution

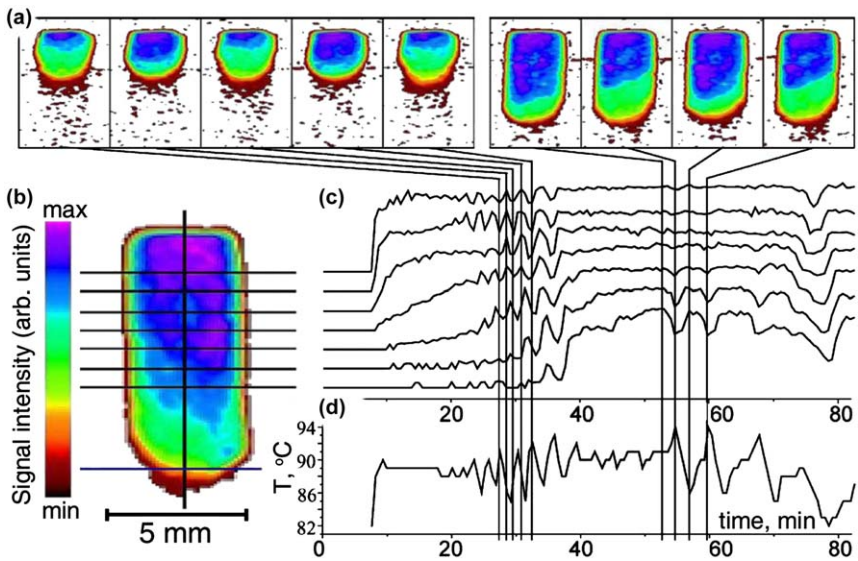

Fig. 7 ^{1}H MRI of an operating single-pellet catalytic reactor during α-methylstyrene hydrogenation. (a) Distribution of the liquid phase within the imaged axial slice of the 1% Pd/γ-Al_2O_3 pellet 4.5 mm in diameter and 12 mm long. (b) One of the images shown together with the signal intensity scale. The intersections of the set of equidistant horizontal lines with the vertical axial line define the spatial locations for the data shown in (c). The bottom horizontal line indicates the level at which the thermocouple is implanted into the pellet. (c) Signal intensity (liquid content) *vs.* time for the spatial locations shown in (b). Vertical lines indicate when the specific images shown in (a) were detected. (d) Temporal behavior of the pellet temperature measured at the location indicated with the bottom horizontal line in (b). Color is available in the electronic version of this figure. Reproduced from ref. 121 with permission of Elsevier BV.

Downloaded from http://books.rsc.org/books/edited-volume/chapter-pdf/1688710/bk9781849739191-00001.pdf by guest on 03 October 2023

observed experimentally were caused by the differences in the rates of heat and mass transfer and phase transitions. In particular, the calculated temperature variations and their period were in agreement with those observed experimentally, including the phase shift between the oscillations of temperature and liquid content.

MRI was also applied successfully to study mass transport processes in operating packed bed reactors. Such studies can address processes that require a cooperative action of a group of pellets not possible in a single catalyst pellet and thus take place on larger length scales. The advantage of MRI is that studies on these larger length scales can provide the spatially resolved information about liquid distribution in the reactor while still providing access to the distributions within each individual catalyst particle. The first studies addressed hydrogenation of olefins in a relatively regular bed of 1% Pd/γ-Al_2O_3 catalyst beads *ca.* 4 mm in diameter.[13,32,35,120] Liquid distribution was thus visualized both within the entire bed and in each individual bead, revealing a number of dynamic phenomena. On the length scale of the bed, distribution of the liquid phase was much less uniform under reactive conditions than in the absence of the reaction, and in addition was altered by interrupting and then restarting the flow of liquid reactant. On the length scale of individual catalyst pellets, the possibility of an ignition of an individual catalyst pellet was observed, which could remain essentially dry for prolonged periods of time even if surrounded by liquid-filled neighbors. In partially dry catalyst beads, a sharp liquid front and its oscillating motion were reminiscent of the behavior observed in the MRI studies on individual catalyst pellets. The redistribution of the liquid phase into the partially dry catalyst beads from the liquid-containing neighbors was visualized. This potentially makes such local structures very efficient in the hydrogenation reaction, as a substantial area of dry catalyst coexists with significant nearby pools of the liquid reactant.

Beds of smaller catalyst beads were used in the hydrogenation of various substrates (AMS, 1-octene, 1-heptene).[13,32,35,120] The distribution of the liquid phase in the individual catalyst beads was still available for the 2–3 mm beads, but not for the 1 mm ones. In the latter case, the steady-state distributions of the liquid phase on the length scale of the bed were not changing in time and revealed the presence of dry areas which were larger for lower liquid flow rates. These distributions depended on whether the catalyst bed was dry or prewetted at the time when the liquid supply was turned on. Under certain conditions, rapid drying indicative of the runaway of the trickle bed was observed.

Another approach for significantly reducing imaging times often used in medical MRI is the implementation of rapid imaging techniques that are able to detect a large number of data points in the *k*-space after each application of the pulse sequence. Unfortunately, most of the rapid pulse sequences developed for medical MRI are not applicable to the studies of liquids in porous materials due to the very different relaxation properties of such liquids compared to soft tissues of an organism. Very short T_2^* times of the liquid phase in porous solids often require the use of spin-echo – based sequences. Therefore, more recent studies[16,36,37,97,98,124]

Downloaded from http://books.rsc.org/books/edited-volume/chapter-pdf/1688710/bk9781849739191-00001.pdf by guest on 03 October 2023

introduced a fast multiecho imaging sequence that could be used to detect 3D images of the bed in 20–30 s or 2D images of one or several slices of the bed in 2–3 s. This approach was used to study in detail the dynamics of the liquid phase redistribution in regular layers of spherical catalyst grains. The results confirmed the existence of partially wet catalyst grains over long periods of time, replenishment of dry or partially wet grains with a liquid from adjacent grains, and the fluctuating liquid front propagation in partially wet grains. Evidently, the observation of such effects is impossible in a model system without an actual reaction.

Periodic modulation of the liquid reactants feed can lead to increased reactor productivity,[125] and MRI can be used to reveal the processes which lead to higher conversions.[124,126] In particular, hydrogenation of 1-octene was used to demonstrate the applicability of MRI in such studies.[124] The distribution of the liquid phase within the catalyst bed during the periodic feed of 1-octene and a continuous feed of H_2 was visualized in the bed comprised of 1% Pd/γ-Al_2O_3 catalyst beads with diameters 1 mm, 2–3 mm, or 4.2 mm. The effects of the liquid flow rate and the period of the on-off cycle of liquid 1-octene supply were studied, and the significant influence of reactant feed modulation on the liquid holdup and catalyst wetting efficiency were visualized directly for the first time through detection of 2D MR images. For continuous supply of 1-octene, the liquid phase distribution was relatively uniform and stationary. In contrast, the bed was largely dry, the distribution of the liquid phase was changing in time and the amount of liquid in the bed was oscillating when 1-octene supply was periodically modulated. Longer periods of liquid feed modulation led to larger liquid contents in the bed during the liquid pulse but also to a substantial or even complete drying of the bed between the pulses. The internal wetting efficiency of the catalyst was found to be lower for the periodic modulation of 1-octene feed as compared to the continuous one. Independent measurements of catalyst temperature and 1-octene conversion demonstrated significant intensification of the hydrogenation process in the periodic regime as compared to the continuous supply of 1-octene. Based on the MRI results, the intensification of the reaction for the periodic feed regime was explained by the reduction of the transport resistance for the H_2 gas and faster hydrogenation of 1-octene in the gas phase as compared to liquid phase hydrogenation.

Another example of an MRI study of an exothermic heterogeneous catalytic reaction is the decomposition of hydrogen peroxide (H_2O_2). MRI studies using a single Fe/Al_2O_3 catalyst pellet[127] revealed chaotic motion of the intrapellet liquid caused by gas and heat evolution during the reaction. Only relatively slow changes in the liquid phase distribution could be monitored as image acquisition time was *ca.* 4 min. In another study,[28,119] a composite pellet consisted of two parts, with one part representing the Ag/γ-Al_2O_3 catalyst with a moderate activity in the reaction while the other one made of γ-Al_2O_3 didn't contain any silver. The pellet was initially filled with water and then placed in the solution of H_2O_2 (0.03–3 M). The NMR signals were detected separately for the two parts of the pellet using spatially selective excitation. It was established that

Downloaded from http://books.rsc.org/books/edited-volume/chapter-pdf/1688710/bk9781849739191-00001.pdf by guest on 03 October 2023

under the experimental conditions, hydrogen peroxide did not diffuse into the catalytically active part of the pellet and the decomposition of H_2O_2 occurred only in a thin surface layer of the pellet. Velocities of convective transport of the liquid phase around the catalyst pellet induced by gas evolution during the reaction were mapped as well.[119] A more recent study addressed reaction-induced transport of the liquid phase around the catalyst pellet during decomposition of H_2O_2 over a Cu- or Pt-doped Al_2O_3 pellet.[128] The temporal evolution of effective diffusion (dispersion) coefficients in the vertical and horizontal directions was addressed using pulsed-gradient stimulated echo (PGSTE) and double-PGSTE experiments. Comparing the results obtained with two techniques, the authors concluded that on the time scale of 10–90 ms stochastic transport played a minor role as compared to random stationary flow. The Pt-based catalyst exhibited a more efficient liquid transport and a shorter time to reaction completion. The T_2 time of the detected ^{1}H NMR signal was shown to change as the reaction proceeded and thus could be also used to qualitatively monitor its progress.[129]

In the context of wastewater bioremediation research, reduction of Cr(VI) was studied in a MRI-compatible reactor.[130] Matrix-immobilized biofilm produced by Serratia sp. bacteria was first used to reduce Pd(II) to produce biofilm-immobilized Pd nanoparticles and then used for reduction of Cr(VI) with formate as the electron donor. The fact that Cr(III) is paramagnetic was employed to monitor the reduction of Cr(VI) to Cr(III) with MRI and to evaluate local concentrations of Cr(III)(aq) in the reactor.

MRI is also increasingly used to study formation, spatial distribution and removal of water in model PEM (proton exchange, or polymer electrolyte, membrane) fuel cells under operating conditions.[131–133]

5.2 Spatially resolved NMR spectroscopy

An important advantage of magnetic resonance is the fact that in essence it is a spectroscopic technique. In the experiments performed using the imaging modality, the spectroscopic information is usually ignored and/or unavailable, *i.e.*, an image often reflects the distribution of the liquid phase irrespective of its composition. Nevertheless, it is possible to recover spectroscopic information from a properly designed spatially resolved MR experiment. This allows one, at least in principle, to obtain spatially resolved quantitative information on conversion and selectivity during catalytic processes. Several general approaches are available for such studies. In chemical shift selective imaging (CSSI), an image is constructed using one particular NMR signal in an NMR spectrum. This approach may be relatively fast, but it loses the rest of the spatial and spectroscopic information. In addition, it is not always possible to selectively excite and/or detect a single NMR line if it overlaps with other spectral components. Another approach, termed chemical shift imaging (CSI), retains all the spectroscopic information and yields a separate NMR spectrum for each pixel (voxel) of an image. Since the spectroscopic information is acquired by detecting a free induction decay (FID) or an echo signal in the absence of any applied gradients, spatial information

Downloaded from http://books.rsc.org/books/edited-volume/chapter-pdf/1688710/bk9781849739191-00001.pdf by guest on 03 October 2023

has to be addressed using phase encoding of the signal, which can make the experiment quite lengthy. If spectroscopic information is desired only for a small number of selected volume elements, volume-selective NMR spectroscopy (VOSY) is a better choice because it reduces the acquisition time as compared to the CSI approach.

The CSI method was applied to study the gas-liquid-solid hydrogenation of AMS to cumene in an operating trickle bed reactor packed with 1% Pd/γ-Al_2O_3 catalyst beads 1 mm in diameter.[13,16,32,98,121] While in modern liquid state high-resolution NMR the signals can have line widths below 1 Hz, they are often much broader for liquids in porous materials. This is caused by the large inhomogeneity of the local magnetic fields induced by the magnetic susceptibility differences between different phases (solid, liquid, and gas), and also by the reduced nuclear spin relaxation times of intrapore liquid. For AMS in the catalyst bed, the ^{1}H NMR spectra detected at 300 MHz exhibited resonances *ca.* 300 Hz wide at 130 °C. Nevertheless, the chemical shift differences between the peaks of AMS and cumene are large enough for the corresponding signals of the two compounds in the pores of alumina to be distinguished. CSI was used to obtain spectroscopic information for each pixel of a 2D image of a 2 mm thick axial slice within the catalyst bed. Essentially, a ^{1}H NMR spectrum was made available for each image pixel. The expected increase in conversion of AMS to cumene down the catalyst bed was observed, and in addition the AMS/cumene ratio was observed to vary in the radial direction (Fig. 8).

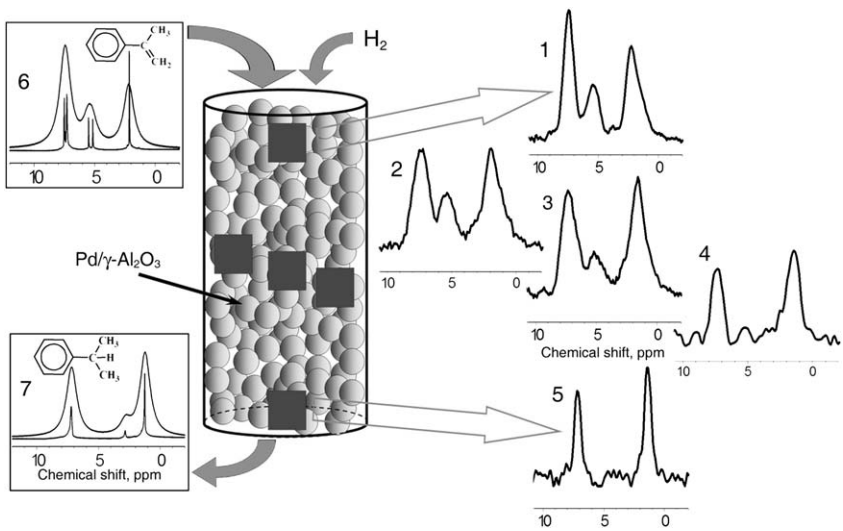

Fig. 8 ^{1}H NMR spectra detected with spatial resolution during AMS hydrogenation in a bed of 1 mm Pt/γ-Al_2O_3 catalyst beads. Each spectrum corresponds to a $170\times330\times2000\ \mu m^3$ voxel. Spectra 1,3,5 correspond to the same radial position within the operating reactor and are detected in its top, middle and bottom parts, respectively, while spectra 2-4 correspond to voxels at the same vertical position in the operating reactor but shifted horizontally by 1.3 mm relative to each other. In the spectra 6 and 7, the traces with narrow lines were detected for liquid AMS (6) and cumene (7), while the traces with broad lines were obtained by mathematically broadening the experimentally observed lines to 300 Hz.

Downloaded from http://books.rsc.org/books/edited-volume/chapter-pdf/1688710/bk9781849739191-00001.pdf by guest on 03 October 2023

One possibility to overcome the problem associated with severe line broadening is to perform an MR experiment using nuclei other than ^{1}H. In particular, the chemical shift range for ^{13}C NMR is at least an order of magnitude larger than that for ^{1}H NMR. Unfortunately, the price to pay when switching from ^{1}H signal detection to other nuclei is an inevitable loss in SNR. This is particularly true for ^{13}C, in part due to a four-fold lower magnetogyric ratio, but mostly because the natural abundance of the ^{13}C isotope is only *ca.* 1.1 %, while the main isotope of carbon (^{12}C) is NMR-silent. As a result, the sensitivity of ^{13}C NMR at natural abundance of the ^{13}C isotope is lower by a factor of $\sim$5870 as compared to ^{1}H NMR. Such dramatic loss in sensitivity can be avoided by using ^{13}C-enriched compounds in the experiments. However, the amounts that one would need to feed a trickle bed reactor for a reasonable period of time would be unacceptably expensive.

In many NMR experiments, polarization is transferred between coupled nuclear spins by means of appropriate NMR pulse sequences. Polarization of spins in a magnetic field is proportional to the magnetogyric ratio of a nucleus, and is therefore *ca.* 4 times larger for ^{1}H as compared to ^{13}C spins. This can be used for a matching enhancement of ^{13}C NMR by transferring polarization from ^{1}H to ^{13}C nuclei. Combination of a 1D MRI experiment and the ^{13}C DEPT (distortionless enhancement by polarization transfer) spectroscopy pulse sequence was used in the studies of 1-octene transformations in the presence of H_2 in a gas-liquid fixed bed model reactor operated under conditions of co-current gas-liquid downflow.[7,81,134] The catalyst bed comprised 1 wt% Pd/Al_2O_3 catalyst trilobes. In this 2D spatial-spectral experiment, ^{13}C NMR spectra were obtained at each axial position along the reactor with a spatial resolution of 3 mm, with the NMR signal intensities integrated in the radial direction. The data acquisition time was *ca.* 17 min. From the analysis of the spatially resolved spectra it could be established that 1-octene readily isomerized into 2-octene, and n-octane was formed upon double bond hydrogenation. At higher flow rates of H_2, 3- and 4-octenes were produced in significant quantities. The concentrations of 1-octene, 2-octene and octane were shown to reach their steady-state values at different axial positions after reactor start-up using the same experimental approach. In a recent study, the novel reactor design mentioned earlier[15] was used to study oligomerization of ethylene at 100–200 °C.

MRI was also employed to study liquid-solid heterogeneous catalytic reactions. One of the early examples is the liquid-phase esterification of methanol and acetic acid into methyl acetate and water performed at room temperature in a packed bed reactor containing small beads of an acidic ion exchange resin.[7,135] To obtain spatially resolved information on chemical conversion, either CSI with one spatial coordinate along the bed axis or VOSY with 30 selected volume elements were applied. Only the NMR signal of the interparticle liquid phase contributed to the acquired data. The conversion of reactants to products was observed to increase along the bed and to decrease with increasing liquid flow rate. In the transverse direction, variations of conversion as large as $\sim$20% could be observed. In the later studies, liquid flow velocities in the bed were

Downloaded from http://books.rsc.org/books/edited-volume/chapter-pdf/1688710/bk9781849739191-00001.pdf by guest on 03 October 2023

both measured under non-reactive conditions using MRI and calculated using the lattice-Boltzmann approach, and then the transport data were correlated with the data on conversion provided by the MRI experiments.[21]

The spectroscopic approach used in the studies of esterification reaction[7,21,135] was based on the detection of the ^{1}H NMR signals of the OH groups of water, acetic acid and methanol which give a single exchange-broadened and shifted NMR line due to the fast proton exchange. In a later study, an approach based on the spectroscopically resolved CSI was demonstrated for an enzymatically catalyzed esterification of propionic acid and 1-butanol into butyl propionate and water carried out on an individual calcium alginate bead containing an immobilized enzyme.[136] The reaction within the alginate bead was monitored by detecting the spectra spatially resolved along one spatial coordinate. The increase in the signals of water and butyl propionate and decrease in the intensity of the butanol signal with time were clearly observed.

The competitive liquid phase etherification of 2-methyl-2-butene (MB) into tert-amyl methyl ether (TAME) and its hydration to tert-amyl alcohol (TAOH) in a fixed bed of H^{+} ion-exchange resin beads was addressed in ref. 7. The 3D experiments performed had two spatial and one spectral coordinates, so that even with the use of the ^{13}C DEPT signal enhancement and a moderate spatial resolution (2.5 mm$\times$3.75 mm) the reaction had to be run for 16 hours to acquire the entire spectral-spatial data set. The spectral resolution was sufficient to evaluate conversion of MB and selectivity to TAME and their variations in the axial and transverse directions.

The spatially resolved ^{13}C DEPT spectroscopy experiment was also used to quantify the composition of the interparticle liquid phase along the reactor in the continuous liquid phase esterification of acetic acid and ethanol to ethyl acetate and water over an ion-exchange resin at ambient temperature and pressure.[137] In the same study, both the intra- and interparticle molecular diffusivities were evaluated separately for different components of the reacting mixture and with a spatial resolution of 6 mm along the catalyst bed. The results demonstrated that in all imaged parts of the bed, the concentration of ethyl acetate was higher in the intraparticle liquid than in the liquid phase outside the particles, indicating that the reaction was mass transfer limited. The total acquisition time of the spatially and chemically resolved diffusion experiment was $\sim$54.5 h.

5.3 Spatially resolved NMR thermometry

Heat transport processes can have an important influence on the operation of a catalytic reactor, and therefore need to be addressed in the experimental studies. This implies that the spatial distribution of temperatures and their variation in time need to be detected. Conventional thermometry techniques are either invasive and provide temperature readings for a limited number of spatial locations (local measurements with thermocouples or other probes[138–141]) or can only probe temperature fields at or near the catalyst or reactor surface (*e.g.*, IR

Downloaded from http://books.rsc.org/books/edited-volume/chapter-pdf/1688710/bk9781849739191-00001.pdf by guest on 03 October 2023

thermography[142–147]). In general, the signals detected in NMR are sensitive to temperature, and therefore NMR/MRI can be used to measure temperatures indirectly. This is currently used in both analytical and biomedical applications of NMR and MRI.[28,148–151] In the high-resolution NMR of liquids, sample temperature is usually determined based on the property of the chemical shifts of certain liquids to appreciably change in response to temperature variation. For instance, ethylene glycol ($HOCH_2CH_2OH$) is one of the well-known NMR ''thermometers''. The chemical shifts of its two NMR signals depend differently on temperature, and therefore their separation provides an accurate evaluation of sample temperature with no need for any additional calibration. NMR thermometry can be also based on other characteristics of liquids and their NMR properties that are sensitive to temperature. In particular, NMR signal intensity, nuclear spin relaxation times, and diffusivity of molecules all depend on local temperature and can be evaluated using NMR. They all were employed in various studies to implement NMR-based thermometry. Unfortunately, none of the four temperature-dependent characteristics mentioned above (chemical shift, signal intensity, relaxation times, and diffusivity) are suitable for temperature measurements of liquids in operating multiphase reactors. Indeed, as demonstrated above, the local liquid contents may change drastically in space and time in an operating reactor, which affects all those temperature-sensitive characteristics even if local temperatures remain unchanged. A straightforward solution to this problem is to enclose a liquid in a small non-metallic container with impermeable walls and place it in a reactor. This strategy was implemented in ref. 81 to evaluate local temperatures during hydrogenation of 1-octene in a bed of Pd/Al_2O_3 trilobes. Four glass bulbs 4 mm in diameter filled with ethylene glycol were placed in various parts of the bed, and volume-selective ^1H NMR spectra of ethylene glycol in these bulbs were detected. Variations of local temperatures in the operating catalyst bed were evaluated with the accuracy of *ca.* $\pm 2\ ^\circ C$. However, this approach is invasive and provides temperature readings in a very limited number of locations within the bed, while an increase in the number of such temperature probes in the bed may significantly perturb reactor behavior. Even more importantly, this approach measures the temperature of a fairly large foreign object, which can be quite different from that of the solid catalyst or the fluid phases in the reactor.

To evaluate the catalyst temperature by NMR, it would be desirable to address the solid phase directly. This requires the detection of the NMR signal of the nuclei of the solid material (catalyst, support). Among the advantages of such approach are the eliminated need to introduce any temperature sensors and the fact that the bulk solid phase remains unchanged during the reaction and thus provides an NMR signal which should be sensitive to temperature variations only. While NMR/MRI of solid materials is often associated with much lower sensitivity as compared to the studies on liquids, some solids and their nuclei can be imaged using conventional MRI approaches.[29–37] Of particular interest in this context is the ^{27}Al nucleus of Al_2O_3 which is often used as a support

Downloaded from http://books.rsc.org/books/edited-volume/chapter-pdf/1688710/bk9781849739191-00001.pdf by guest on 03 October 2023

for heterogeneous catalysts. Indeed, both the relaxation times and the signal intensity of ^{27}Al nuclei of γ-Al_2O_3 are sensitive to temperature.[16,30,98,122] Based on this fact, ^{27}Al MRI was applied to reveal spatial and temporal temperature variations in an operating catalytic reactor.[98,152] In the experiment, a mixture of propylene and H_2 was supplied to a fixed bed of Pd/γ-Al_2O_3 catalyst. One-dimensional profiles of the ^{27}Al NMR signal intensity along the catalyst bed with a sub-mm spatial resolution were detected every 3 minutes. The temperature of the bed was varied by changing the flow rate of propylene while keeping the H_2 feed constant. Thermocouple measurements in the lower part of the bed showed that the catalyst temperature increase from room temperature to 250 °C was accompanied by the decrease in the ^{27}Al NMR signal of the alumina support. Under certain regimes, the signal intensity distribution along the catalyst bed was significantly non-uniform, which likely reflected the gradient in the catalyst temperature. Control experiments performed at various temperatures demonstrated that ^{27}Al NMR signal intensity of alumina was insensitive to the composition of the gas phase in contact with the catalyst, confirming that signal intensity can be used as a measure of the catalyst temperature.

The ^{27}Al MRI thermometry approach was recently extended from the 1D qualitative imaging of temperature distribution to a 2D quantitative temperature mapping.[153] A single cylindrical Pt/γ-Al_2O_3 pellet was used to perform catalytic oxidation of H_2 with O_2 (Fig. 9). The pellet (4.2 mm in diameter and *ca.* 1 cm long) was glued to the wall on the inside of a 10 mm glass tube reactor. The transverse images visualized the geometry of the experiment since both the glass tube and the catalyst contain ^{27}Al

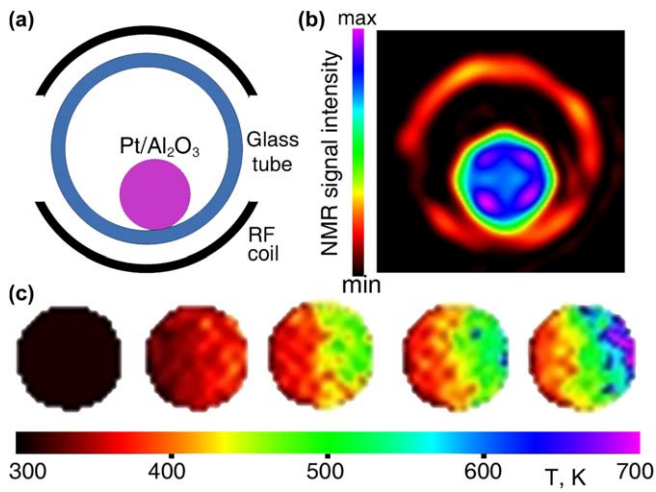

Fig. 9 (a) Geometry of Pt/Al_2O_3 pellet positioning for the MRI thermometry experiment during catalytic gas phase oxidation of H_2. (b) 2D ^{27}Al MR image of the catalyst pellet and the reactor glass tube. (c) 2D temperature maps of the catalyst pellet derived from the images of the catalyst pellet detected at different H_2 flow rates using the calibration curve that relates the ^{27}Al NMR signal intensity to the actual temperature of alumina. Color is available in the electronic version of this figure.

Downloaded from http://books.rsc.org/books/edited-volume/chapter-pdf/1688710/bk9781849739191-00001.pdf by guest on 03 October 2023

nuclei and thus contribute to the image. At the same time, the signal of glass was much weaker than that of the catalyst pellet, and could be neglected in the temperature mapping experiments. The ^{27}Al NMR signal intensity was uniform across the catalyst pellet in the absence of H_2. Once the H_2 flow was started, the signal decreased and exhibited a gradient in the pellet in the direction toward the contact between the pellet and the tube wall. Both effects became more pronounced as the H_2 flow rate was increased further. As the acquisition time of each 2D ^{27}Al MR image with the 0.4 mm×0.4 mm in-plane spatial resolution (without slice selection) and an acceptable SNR was fairly long (21 min), the H_2 flow rates were changed only between image acquisitions to achieve steady-state conditions.

An independent calibration experiment was used which related the measured ^{27}Al NMR signal intensity of alumina to its actual temperature which was measured by a thermocouple. This was used to convert the obtained images into quantitative 2D temperature maps. These maps revealed a pronounced temperature gradient in the transverse plane of the catalyst pellet associated with its asymmetric positioning in the reactor. Catalyst temperatures up to 700 K were achieved, demonstrating the applicability of this approach to the studies of high-temperature processes. The uncertainties in the temperature evaluation were governed by the MR signal measurement noise and were estimated as *ca.* 10–12 K at 400 K, *ca.* 30 K at 500 K and even larger at higher temperatures. This trend is explained by the overall decrease in the measured signal intensity with increasing sample temperature. It is reasonably straightforward to extend this approach to the thermometry of multiple catalyst pellets and packed catalyst beds. Since the experiment does not use any solid-state imaging methods and hardware, it can be implemented relatively easily on many instruments equipped with pulsed magnetic field gradients, including the *ex situ*, inside-out or mobile MRI devices developed recently,[11,154,155] which could be the next step to thermometry of operating industrial reactors. It is essential that this approach allows one to evaluate the true temperature of the solid catalyst pellets and packed beds in a non-invasive manner and with spatial resolution.

Despite the sensitivity problems associated with the direct detection of the signal of a solid phase, ^{27}Al NMR/MRI of alumina appears to be a useful temperature sensor. However, this approach is not problem-free as well. For some other Al-containing materials including zeolites, this approach may fail since surface adsorption processes may significantly affect the ^{27}Al NMR signal intensity. Higher temperatures lead to lower signal intensities, reducing the sensitivity and achievable spatial resolution and/or increasing measurement time. The approach also needs an independent calibration of signal intensity *versus* temperature for the measurements to be quantitative. Nevertheless, the results already obtained are quite encouraging and demonstrate that non-invasive solid state MRI thermometry is feasible in favorable cases, and may become a useful technique capable of revealing temperature gradients and formation and evolution of hot spots in operating catalytic reactors. An extension to liquid-solid and gas-liquid-solid processes should be

Downloaded from http://books.rsc.org/books/edited-volume/chapter-pdf/1688710/bk9781849739191-00001.pdf by guest on 03 October 2023

straightforward as the presence of a liquid should not affect the ^{27}Al NMR signal in any way other than through the catalyst temperature.

5.4 MRI of microreactors and catalytic signal enhancement

One of the recent trends in chemical technology and catalysis is the use of microreactors and microfluidic devices. Their growing popularity is attributed to a number of advantages that include a better control over mass and heat transport, enhanced performance, faster and more efficient chemical processes, improved safety even when operated under extreme conditions, and easier scale-up. At the same time, from the point of view of NMR and MRI studies, microdevices present some additional challenges. In a conventional NMR/MRI experiment, the size of an rf coil would be dictated by the external size of such device, which is often much larger than the characteristic dimensions of the reaction zone of a microreactor or the channel diameters of a microfluidic chip. The low filling factor of the rf coil results in a poor SNR for liquids and makes such experiments essentially unfeasible for gases.

A useful approach particularly suitable for addressing gas-phase reactions in microreactors is based on the so-called remote detection (RD) method.[90,94,156–158] The idea behind it is to separate the encoding and the detection parts of NMR pulse sequence both in space and time. The large rf coil in which a microreactor or a microchip resides is used for encoding the spatial information into the longitudinal magnetization of the fluid in the voids or channels. The fluid flows out of the reactor continuously through a thin capillary which passes through a microcoil used for a periodic detection of the NMR signal. In addition to spatial and spectroscopic information, the time-of-flight information is obtained using a set of delays between the encoding event and the multiple detection events to recover the temporal data.

In ref. 159 RD was used to address hydrogenation of propylene in a microreactor comprising 36 parallel channels with a $50\times50\,\mu m^2$ cross-section and 5, 10 or 20 mm long, produced by etching a silicon wafer. The channel walls were coated with a Pt layer. The microreactor was placed in a 25 mm i.d. rf coil located in a 7.05 T NMR magnet. The detection microcoil was wound directly around the 360 μm o.d. outlet capillary and was 3 mm long and located *ca.* 1 cm below the encoding coil. The proximity of the detection microcoil to the magnet center ensures the reasonable homogeneity of the static magnetic field at its location provided by the shimming system of the NMR magnet. It also leads to relatively short travel times of the gas from the encoding to the detection region which reduces the relaxation-induced losses. After each repetition of the encoding part of the pulse sequence, 30 consecutive FIDs were collected, separated by a 21 ms delay. With the spatial resolution of 2D images obtained (1.9 mm along the channels and 0.5–1 mm in the transverse direction), each pixel covered 2–5 individual channels in the transverse direction. Despite the small dimensions of the microcoil (53 nl of gas in the detection volume), the NMR spectrum of the gas mixture could be detected. The line width for the static gas was *ca.* 30 Hz and increased to *ca.* 100 Hz when the gas was flowing because the gas residence time in

Downloaded from http://books.rsc.org/books/edited-volume/chapter-pdf/1688710/bk9781849739191-00001.pdf by guest on 03 October 2023

the microcoil was *ca.* 20 ms at the chosen flow velocity. This was sufficient to resolve the chemical shifts of the reactant (propylene) and the product (propane). From the set of spatially phase-encoded spectra, a set of images could be reconstructed, with each image in the set depicting the spatial location of the chosen compound with a given time-of-flight (TOF) to the detection microcoil. Such TOF images were extracted for both propylene and propane. From these images it was concluded that gas flow velocities and propylene conversions were different in different parts of the reactor, with smaller flow rates providing larger product yields. The interpretation of the RD CSI experiment results can be rather non-trivial. The authors demonstrated, however, that a detailed understanding of the experiment combined with an appropriate choice of the pulse sequence parameters can provide the true TOF images of the reaction product. Possible ways to improve the sensitivity of the experiment were discussed, which may lead to the spatial resolution sufficient to resolve individual channels.

The limited sensitivity is a major obstacle for improving the spatial and temporal resolution in most existing MRI experiments, and is also a significant obstacle for developing novel powerful tools for the MRI toolkit. Imaging of gases and visualization of narrow channels at high spatial resolution are particularly demanding in this respect. It was estimated[159] that the use of the microcoil for signal detection in the RD experiments improved the detection sensitivity by a factor of *ca.* 800 compared to a hypothetical experiment in which the large encoding rf coil would be used for signal detection. Nevertheless, further improvement in SNR would be highly desirable not only for the studies of microreactors, but also to address larger model reactors as well. In fact, the entire field of NMR/MRI can significantly benefit from an improved SNR. It is therefore not surprising that the so-called hyperpolarization methods[2,28,160–173] are becoming extremely popular in magnetic resonance. This family of techniques is being developed in an attempt to maximize the polarization of nuclear spins in a magnetic field, thereby providing signal enhancements of up to 2×10^4 for ^{1}H NMR/MRI in a 14 T field (600 MHz NMR instrument), and even higher enhancements at lower fields and/or for other nuclei.

One of the hyperpolarization techniques, called parahydrogen-induced polarization (PHIP, or PASADENA) is particularly suitable for the development of hypersensitive NMR/MRI tools for catalysis. This is a rare example of a situation when catalysis can help magnetic resonance to solve its problems, while usually it is the other way around. Signal enhancement with PHIP[2,174–179] is based on a catalytic hydrogenation reaction in which parahydrogen (pH_2) is used instead of normal H_2. Parahydrogen is one of the two nuclear spin isomers of H_2 with the total nuclear spin of two H atoms $I=0$. It gives no NMR signal by itself, but the highly correlated state of its nuclear spins can be converted into an NMR signal enhancement. To achieve this, the equivalence of the two H atoms of the H_2 molecule has to be broken, which can be achieved when pH_2 participates in a suitable chemical reaction. PHIP is observed in many homogeneous hydrogenation reactions of suitable unsaturated

Downloaded from http://books.rsc.org/books/edited-volume/chapter-pdf/1688710/bk9781849739191-00001.pdf by guest on 03 October 2023

precursors catalyzed by transition metal complexes. Since in PHIP the hyperpolarization of nuclear spins is produced in a catalytic reaction, this technique can be used as a highly sensitive NMR-based tool for the studies of the mechanisms and kinetics of homogeneous hydrogenations catalyzed by transition metal complexes in solution.[180–182] The high sensitivity provided by PHIP enables the detection not only of reaction products, but also of short-lived reaction intermediates that are normally present in solution at very low concentrations and thus escape NMR detection.

More recently, it has been demonstrated that PHIP effects can be also observed in heterogeneous hydrogenations of unsaturated substrates catalyzed by transition metal complexes immobilized on suitable porous solid supports[178,179,183–186] as well as by supported metal nanoparticles.[178,179,187] The latter observation was quite surprising as metal surfaces were expected to be unable to achieve the required incorporation of both H atoms of a H_2 molecule into the same product molecule because of the dissociative chemisorption of H_2 and rapid surface migration of the resulting H atoms. Nevertheless, PHIP effects were successfully observed in hydrogenation reactions catalyzed by many supported metal catalysts.[178,179,188–191] This provides an opportunity for the development of a powerful hypersensitive NMR-based technique for the characterization of the heterogeneous catalytic processes of practical importance.

Combination of PHIP with MRI was already used to study processes in a model catalytic reactor.[98,178,192] A small packed bed reactor comprised a piece of tubing packed with a heterogeneous Rh-based catalyst. The reactor was positioned inside the NMR probe and was imaged during the hydrogenation of propylene with parahydrogen. Those parts of the catalyst bed where the hydrogenation of propylene to propane was taking place were visualized in the images as the regions with hyperintense NMR signal. Furthermore, the signal enhancement provided by PHIP made it possible to detect the velocity map for the hydrocarbon gas flowing in the packed bed of the operating reactor. The experiments demonstrated that both the catalyst packing and the flow field were spatially non-uniform.

PHIP-enhanced MRI in combination with the RD technique considered above was used to address packed bed microreactors.[193] Three different continuous flow microreactors packed with Rh/SiO_2 catalyst were used in the experiments. The diameters of the packed beds were 800, 405, and 150 μm, and their lengths were 5, 14, and 15 mm, respectively. The signal enhancement provided by PHIP in the hydrogenation of propylene to propane using pH_2 was estimated as *ca.* 60, and the overall sensitivity enhancement factor given by RD (820) and PHIP was estimated as *ca.* 5×10^4. The NMR signal of the hyperpolarized gas (propane) significantly exceeded that of the thermally polarized gas (propylene), which simplifies the interpretation of the results of the RD experiment. The average gas flow rates, both in the packed bed and in the outlet capillary, were determined from the 2D data sets with one spatial (axial) and one TOF coordinate, directly from the slope of the corresponding ridges.

Downloaded from http://books.rsc.org/books/edited-volume/chapter-pdf/1688710/bk9781849739191-00001.pdf by guest on 03 October 2023

Comparison of the gas flow velocities and signal intensities in the packed bed and in the outflow capillary revealed a substantial adsorption of the gas on the porous catalyst support in the packed bed, which was then quantified. Furthermore, summation of all 1D axial profiles over the TOF coordinate provided the axial distribution of propane concentration assuming that the packed bed was uniform and relaxation effects negligible. Such distributions obtained for the three reactors were simulated based on the plug-flow reactor behavior and the appropriate kinetic models. The experiments were further extended to obtain 3D data sets, namely the 2D images detected for different times-of-flight (Fig. 10). The images revealed the plug-like gas flow in the two smaller reactors, while some deviation from the plug-like behavior and a larger dispersion was revealed for the larger one. The build-up of hyperpolarization along the microreactor can be clearly observed.

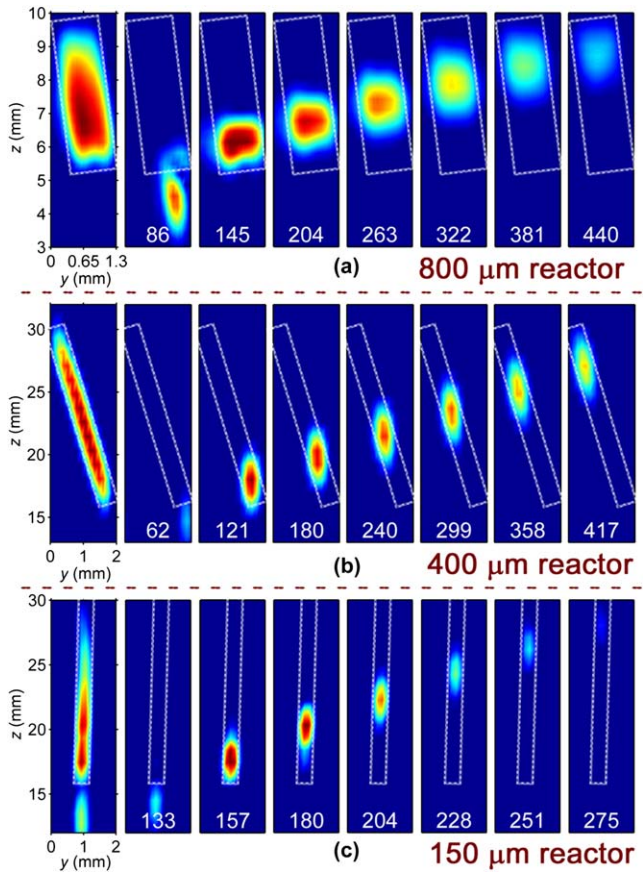

Fig. 10 RD TOF images acquired for Rh/SiO_2 catalyst beds of three different diameters at 60 °C during propylene hydrogenation with parahydrogen. The leftmost images are the time projections obtained by summation of all images shown to their right. Travel times are indicated in the panels in milliseconds. The catalyst bed regions are outlined with white dashed lines. The complete data set for each reactor was acquired in 13 min with a time resolution of 12 ms and a spatial resolution of 160–250 μm in the horizontal direction and 0.62–2.2 mm in the vertical direction. Reproduced from ref. 193 with permission of Wiley-VCH Verlag GmbH & Co. KGaA, Weinheim.

Downloaded from http://books.rsc.org/books/edited-volume/chapter-pdf/1688710/bk9781849739191-00001.pdf by guest on 03 October 2023

6 Summary and outlook

Applications of MR imaging in heterogeneous catalysis and related disciplines are still an art rather than everyday routine. Nevertheless, the technique has reached a stage when it can provide useful data on the processes even in operating model reactors, including information about the internal structure, mass and heat transport processes, and chemical conversion of reactants into products. Given the complexity of processes that take place in the reactors, the most powerful approach is to use MRI in combination with other experimental techniques and mathematical modeling. The data provided by MRI can be used as a direct input to limit the number of unknowns in calculations as well as to validate the results of such calculations. This approach has synergistic potential and is capable of providing significantly more information than MRI studies or modeling alone.[56]

In addition, this field of research holds promise for significant growth in the future, which will be fueled by the ongoing developments in other areas of application of NMR and MRI, in particular in the broad field of porous media MR, where the development of faster imaging techniques and techniques applicable to samples with short T_2 times is highly desirable and attracts a lot of attention at present. Another major problem is insufficient sensitivity which poses significant obstacles on the way to higher spatial and temporal resolution and to the development of novel applications. This calls for the implementation of significant signal enhancement, which can be achieved through the ongoing development of the hyperpolarization techniques. Furthermore, it is already quite clear that the utilization of the properties of the so-called long-lived spin states[194–199] can go a long way in extending the lifetime of hyperpolarization well beyond the T_1 limit and thus can significantly broaden the scope of new and exciting developments. Hypepolarization methods are already being applied to the studies of enzymatic processes *in vivo* and in bioreactors,[2] and thus can provide new impetus for applications of MRI in the studies of model biocatalytic reactors.[200–203]

References

1 I. V. Koptyug, *Appl. Magn. Reson.*, 2007, **32**, 1.
2 I. V. Koptyug, Spin Hyperpolarization in NMR to Address Enzymatic Processes In Vivo, *Mendeleev Commun.*, 2013, in press.
3 P. T. Callaghan, *Principles of Nuclear Magnetic Resonance Microscopy*, Oxford University Press, New York, 1991.
4 B. Blümich, *NMR Imaging of Materials*, Oxford University Press, New York, 2003.
5 R. Kimmich, *NMR: Tomography, Diffusometry, Relaxometry*, Springer-Verlag, Berlin, 1997.
6 I. V. Koptyug and R. Z. Sagdeev, *Russ. Chem. Rev.*, 2002, **71**, 593.
7 L. F. Gladden, M. D. Mantle and A. J. Sederman, *Adv. Catal.*, 2006, **50**, 1.
8 L. Ciobanu, D. A. Seeber and C. H. Pennington, *J. Magn. Reson.*, 2002, **158**, 178.
9 S. K. Kuster, E. Danieli, B. Blumich and F. Casanova, *Phys. Chem. Chem. Phys.*, 2011, **13**, 13172.

Downloaded from http://books.rsc.org/books/edited-volume/chapter-pdf/1688710/bk9781849739191-00001.pdf by guest on 03 October 2023

10 B. Blumich, F. Casanova, M. Dabrowski, E. Danieli, L. Evertz, A. Haber, M. Van Landeghem, S. Haber-Pohlmeier, A. Olaru, J. Perlo and O. Sucre, *New J. Phys.*, 2011, **13**, 015003.
11 B. Blumich, J. Perlo and F. Casanova, *Progr. NMR Spectr.*, 2008, **52**, 197.
12 F. Dalitz, M. Cudaj, M. Maiwald and G. Guthausen, *Progr. NMR Spectr.*, 2012, **60**, 52.
13 A. A. Lysova, I. V. Koptyug, A. V. Kulikov, V. A. Kirillov, R. Z. Sagdeev and V. N. Parmon, *Chem. Eng. J.*, 2007, **130**, 101.
14 N. L. Nguyen, V. van Buren, A. von Garnier, E. H. Hardy and R. Reimert, *Chem. Eng. Sci.*, 2005, **60**, 6289.
15 M. P. Renshaw, S. T. Roberts, M. Lutecki, M. D. Mantle, J. McGregor, A. J. Sederman, L. F. Gladden. Operando MRI: Fixed-bed heterogeneous catalysis at elevated temperature and pressure. Extended abstract, 11th European Congress on Catalysis – EuropaCat-XI, Lyon, France, September 1–6, 2013.
16 I. V. Koptyug, *Encyclopedia of Magnetic Resonance*, ed. R. K. Harris and R. Wasylishen, John Wiley & Sons, Ltd., 2011, emrstm1266.
17 N. L. Nguyen, R. Reimert and E. H. Hardy, *Chem. Eng. Technol.*, 2006, **29**, 820.
18 N. L. Nguyen, V. van Buren, R. Reimert and A. von Garnier, *Magn. Reson. Imaging*, 2005, **23**, 395.
19 A. Feinauer, S. A. Altobelli and E. Fukushima, *Magn. Reson. Imaging*, 1997, **15**, 479.
20 X. Ren, S. Stapf and B. Blumich, *AIChE J.*, 2005, **51**, 392.
21 E. H. L. Yuen, A. J. Sederman, F. Sani, P. Alexander and L. F. Gladden, *Chem. Eng. Sci.*, 2003, **58**, 613.
22 S. P. Sullivan, F. M. Sani, M. L. Johns and L. F. Gladden, *Chem. Eng. Sci.*, 2005, **60**, 3405.
23 P. Jezzard, J. J. Attard, T. A. Carpenter and L. D. Hall, *Progr. NMR Spectr.*, 1991, **23**, 1.
24 D. G. Cory, *Annu. Rep. NMR Spectrosc.*, 1992, **24**, 87.
25 J. B. Miller, *Progr. NMR Spectr.*, 1998, **33**, 273.
26 A. J. Fagan and D. J. Lurie, *Annu. Rep. NMR Spectrosc.*, 2005, **56**, 97.
27 D. E. Demco and B. Blumich, *Concepts Magn. Reson.*, 2000, **12**, 188.
28 I. V. Koptyug and R. Z. Sagdeev, *Russ. Chem. Rev.*, 2003, **72**, 165.
29 I. V. Koptyug, A. A. Lysova, A. V. Khomichev and R. Z. Sagdeev, *Diff. Fundam.*, 2007, **5**, 2–1.
30 I. V. Koptyug, D. R. Sagdeev, E. Gerkema, H. Van As and R. Z. Sagdeev, *J. Magn. Reson.*, 2005, **175**, 21.
31 I. V. Koptyug and A. A. Lysova, *Bruker Spin Report*, 2006, **157–158**, 22.
32 I. V. Koptyug and A. A. Lysova, *NMR Imaging in Chemical Engineering*, ed. S. Stapf and S.-I. Han, Wiley-VCH, Weinheim, 2006, 570–589.
33 M. S. Conradi, *J. Magn. Reson.*, 1991, **93**, 419.
34 I. V. Koptyug, A. V. Khomichev, A. A. Lysova and R. Z. Sagdeev, *Appl. Magn. Reson.*, 2007, **32**, 321.
35 I. V. Koptyug, A. A. Lysova, R. Z. Sagdeev, V. A. Kirillov, A. V. Kulikov and V. N. Parmon, *Catal. Today*, 2005, **105**, 464.
36 I. V. Koptyug, A. A. Lysova, R. Z. Sagdeev and V. N. Parmon, *Catal. Today*, 2007, **126**, 37.
37 I. V. Koptyug, A. A. Lysova, K. V. Kovtunov, V. V. Zhivonitko, A. V. Khomichev and R. Z. Sagdeev, *Russ. Chem. Rev.*, 2007, **76**, 583.
38 J. L. Ackerman, L. Garrido, J. R. Moore, B. Pfleiderer and Y. Wu, *Magnetic Resonance Microscopy. Methods and Applications in Materials Science, Agriculture and Biomedicine*, ed. B. Blumich and W. Kuhn, VCH, Weinheim, 1992, pp. 237–260.

Downloaded from http://books.rsc.org/books/edited-volume/chapter-pdf/1688710/bk9781849739191-00001.pdf by guest on 03 October 2023

39 D. A. Graf von der Schulenburg and M. L. Johns, *Chem. Eng. Sci.*, 2011, **66**, 3003.
40 S. Harms, S. Stapf and B. Blumich, *J. Magn. Reson.*, 2006, **178**, 308.
41 C. R. Muller, D. J. Holland, A. J. Sederman, M. D. Mantle, L. F. Gladden and J. F. Davidson, *Powder Technol.*, 2008, **183**, 53.
42 L. F. Gladden and J. Mitchell, *New J. Phys.*, 2011, **13**, 035001.
43 I. V. Koptyug and R. Z. Sagdeev, *Russ. Chem. Rev.*, 2002, **71**, 789.
44 J. Karger and S. Vasenkov, *Microporous Mesoporous Mater.*, 2005, **85**, 195.
45 C. Chmelik and J. Karger, *Chem. Soc. Rev.*, 2010, **39**, 4864.
46 J. Karger, *Mol. Sieves*, 2008, **7**, 85.
47 F. Stallmach and J. Karger, *Adsorption*, 1999, **5**, 117.
48 P. Kortunov, S. Vasenkov, J. Karger, M. Fe Elia, M. Perez, M. Stocker, G. K. Papadopoulos, D. Theodorou, B. Drescher, G. McElhiney, B. Bernauer, V. Krystl, M. Kocirik, A. Zikanova, H. Jirglova, C. Berger, R. Glaser, J. Weitkamp and E. W. Hansen, *Chem. Mater.*, 2005, **17**, 2466.
49 A. Pampel, M. Fernandez, D. Freude and J. Karger, *Chem. Phys. Lett.*, 2005, **407**, 53.
50 S. Vasenkov, O. Geier and J. Karger, *Eur. Phys. J. E*, 2003, **12**, S35.
51 M. Gratz, M. Wehring, P. Galvosas and F. Stallmach, *Microporous Mesoporous Mater.*, 2009, **125**, 30.
52 I. Ardelean and R. Kimmich, *Annu. Rep. NMR Spectrosc.*, 2003, **49**, 43.
53 F. Stallmach and P. Galvosas, *Annu. Rep. NMR Spectrosc.*, 2007, **61**, 51.
54 I. V. Koptyug, *Progr. NMR Spectr.*, 2012, **65**, 1.
55 E. Fukushima, *Annu. Rev. Fluid Mech.*, 1999, **31**, 95.
56 C. J. Elkins and M. T. Alley, *Exp. Fluids*, 2007, **43**, 823.
57 J. M. Pope and S. Yao, *Concepts Magn. Reson.*, 1993, **5**, 281.
58 J. D. Seymour and P. T. Callaghan, *AIChE J.*, 1997, **43**, 2096.
59 P. T. Callaghan and Y. Xia, *J. Magn. Reson.*, 1991, **91**, 326.
60 I. V. Koptyug, A. A. Lysova, A. V. Matveev, L. Yu. Ilyina, R. Z. Sagdeev and V. N. Parmon, *Magn. Reson. Imaging*, 2003, **21**, 337.
61 S.-I. Han, S. Stapf and B. Blumich, *J. Magn. Reson.*, 2000, **146**, 169.
62 S.-I. Han and B. Blumich, *Appl. Magn. Reson.*, 2000, **18**, 101.
63 B. Blumich, P. T. Callaghan, R. A. Damion, S.-I. Han, A. A. Khrapitchev, K. J. Packer and S. Stapf, *J. Magn. Reson.*, 2001, **152**, 162.
64 A. A. Khrapitchev, S. Han, S. Stapf and B. Blumich, *J. Magn. Reson.*, 2002, **159**, 36.
65 P. T. Callaghan and B. Manz, *J. Magn. Reson. A*, 1994, **106**, 260.
66 I. V. Koptyug, A. A. Lysova, A. V. Matveev, L. Yu. Ilyina R. Z. Sagdeev and V. N. Parmon, *Fluid transport in nanoporous materials*, ed. W. C. Conner and J. Fraissard, Springer, Dordrecht, 2006, 353–374.
67 L. F. Gladden and A. J. Sederman, *J. Magn. Reson.*, 2013, **229**, 2.
68 B. Newling, *Progr. NMR Spectr.*, 2008, **52**, 31.
69 A. K. Heibel, T. W. J. Scheenen, J. J. Heiszwolf, H. Van As, F. Kapteijn and J. A. Moulijn, *Chem. Eng. Sci.*, 2001, **56**, 5935.
70 I. V. Koptyug, A. A. Lysova, A. V. Matveev, V. N. Parmon and R. Z. Sagdeev, *Topics in Catalysis*, 2005, **32**, 83.
71 Y. E. Kutsovsky, L. E. Scriven, H. T. Davis and B. E. Hammer, *Phys. Fluids*, 1996, **8**, 863.
72 D. Mertens, C. Heinen, E. H. Hardy and H. W. Buggisch, *Chem. Eng. Technol.*, 2006, **29**, 854.
73 T. R. Brosten, S. L. Codd, K. V. Romanenko, S. W. Sofie and J. D. Seymour, *AIChE J.*, 2009, **55**, 2506.
74 I. V. Koptyug, S. A. Altobelli, E. Fukushima, A. V. Matveev and R. Z. Sagdeev, *J. Magn. Reson.*, 2000, **147**, 36.

Downloaded from http://books.rsc.org/books/edited-volume/chapter-pdf/1688710/bk9781849739191-00001.pdf by guest on 03 October 2023

75 I. V. Koptyug, L. Yu. Ilyina, A. V. Matveev, R. Z. Sagdeev, V. N. Parmon and S. A. Altobelli, *Catal. Today*, 2001, **69**, 385.
76 I. V. Koptyug, A. V. Matveev and S. A. Altobelli, *Appl. Magn. Reson.*, 2002, **22**, 187.
77 I. V. Koptyug, L. Y. Ilyina, A. V. Matveev, R. Z. Sagdeev and V. N. Parmon, *Magnetic resonance in colloid and interface science*, ed. J. Fraissard and O. Lapina, Kluwer Academic Publishers, Dordrecht, 2002, 197–208.
78 I. V. Koptyug, K. V. Kovtunov, E. Gerkema, L. Kiwi-Minsker and R. Z. Sagdeev, *Chem. Eng. Sci.*, 2007, **62**, 4459.
79 S. Tsushima, S. Hirai, Y. Yamamoto and Y. Nakasuji, *Magn. Reson. Imaging*, 2003, **21**, 430.
80 N. P. Ramskill, L. F. Gladden, A. P. E. York, A. J. Sederman, J. Mitchell and K. A. Hardstone, *Catal. Today*, 2013, **216**, 104.
81 L. F. Gladden, F. J. R. Abegao, C. P. Dunckley, D. J. Holland, M. H. Sankey and A. J. Sederman, *Catal. Today*, 2010, **155**, 157.
82 J. Park and S. J. Gibbs, *AIChE J.*, 1999, **45**, 655.
83 U. Tallarek, D. van Dusschoten, H. Van As, E. Bayer and G. Guiochon, *J. Phys. Chem. B*, 1998, **102**, 3486.
84 U. Tallarek, E. Bayer and G. Guiochon, *J. Am. Chem. Soc.*, 1998, **120**, 1494.
85 U. Tallarek, F. J. Vergeldt and H. Van As, *J. Phys. Chem. B*, 1999, **103**, 7654.
86 U. Tallarek, D. van Dusschoten, H. Van As, G. Guiochon and E. Bayer, *Angew. Chem. Int. Ed.*, 1998, **37**, 1882.
87 J. J. Tessier, K. J. Packer, J.-F. Thovert and P. M. Adler, *AIChE J.*, 1997, **43**, 1653.
88 L. G. Kaiser, J. W. Logan, T. Meersmann and A. Pines, *J. Magn. Reson.*, 2001, **149**, 144.
89 S. L. Codd and S. A. Altobelli, *J. Magn. Reson.*, 2003, **163**, 16.
90 E. Harel, J. Granwehr, J. A. Seeley and A. Pines, *Nature Mater.*, 2006, **5**, 321.
91 A. V. Matveev, L. V. Barysheva, I. V. Koptyug, V. M. Khanaev and A. S. Noskov, *Chem. Eng. Sci.*, 2006, **61**, 2394.
92 K. Kose, *Phys. Rev. A*, 1991, **44**, 2495.
93 A. B. Tayler, D. J. Holland, A. J. Sederman and L. F. Gladden, *J. Magn. Reson.*, 2011, **211**, 1.
94 V. S. Bajaj, J. Paulsen, E. Harel and A. Pines, *Science*, 2010, **330**, 1078.
95 A. A. Lysova, I. V. Koptyug, R. Z. Sagdeev, V. N. Parmon, J. A. Bergwerff and B. M. Weckhuysen, *J. Am. Chem. Soc.*, 2005, **127**, 11916.
96 J. A. Bergwerff, L. G. A. van der Water, A. A. Lysova, I. V. Koptyug, T. Visser, K. P. de Jong and B. M. Weckhuysen, *Stud. Surf. Sci. Catal.*, 2006, **162**, 175.
97 I. V. Koptyug, A. A. Lysova, V. N. Parmon and R. Z. Sagdeev, *Kinet. Catal.*, 2007, **48**, 464.
98 A. A. Lysova and I. V. Koptyug, *Chem. Soc. Rev.*, 2010, **39**, 4585.
99 A. A. Lysova, J. A. Bergwerff, L. Espinosa-Alonso, B. M. Weckhuysen and I. V. Koptyug, *Appl. Catal. A: General*, 2010, **374**, 126.
100 J. A. Bergwerff, A. A. Lysova, L. Espinosa Alonso, I. V. Koptyug and B. M. Weckhuysen, *Angew. Chem. Int. Ed.*, 2007, **46**, 7224.
101 J. A. Bergwerff, A. A. Lysova, L. Espinosa-Alonso, I. V. Koptyug and B. M. Weckhuysen, *Chem. Eur. J.*, 2008, **14**, 2363.
102 L. Espinosa-Alonso, A. A. Lysova, P. Peinder, K. P. de Jong, I. V. Koptyug and B. M. Weckhuysen, *J. Am. Chem. Soc.*, 2009, **131**, 6525.
103 I. V. Koptyug, L. Yu. Khitrina, V. N. Parmon and R. Z. Sagdeev, *Magn. Reson. Imaging*, 2001, **19**, 531.
104 L. Yu. Khitrina, I. V. Koptyug, N. A. Pakhomov, R. Z. Sagdeev and V. N. Parmon, *J. Phys. Chem. B*, 2000, **104**, 1966.

Downloaded from http://books.rsc.org/books/edited-volume/chapter-pdf/1688710/bk9781849739191-00001.pdf by guest on 03 October 2023

105 Z. R. Ismagilov, S. A. Yashnik, A. V. Matveev, I. V. Koptyug and J. A. Moulijn, *Catal. Today*, 2005, **105**, 484.
106 A. von Garnier, E. H. Hardy, J.-M. Schweitzer and R. Reimert, *Chem. Eng. Sci.*, 2007, **62**, 5330.
107 K. Y. Cheah, N. Chiaranussati, M. P. Hollewand and L. F. Gladden, *Appl. Catal. A: General*, 1994, **115**, 147.
108 J.-L. Bonardet, T. Domeniconi, P. N'Gokoli-Kekele, M.-A. Springuel-Huet and J. Fraissard, *Langmuir*, 1999, **15**, 5836.
109 T. Domeniconi, J.-L. Bonardet, M.-A. Springuel-Huet, J. Fraissard and J.-M. Dereppe, *Stud. Surf. Sci. Catal.*, 1997, **111**, 647.
110 N.-K. Bar, F. Bauer, D. M. Ruthven and B. J. Balcom, *J. Catal.*, 2002, **208**, 224.
111 S. Stapf, X. Ren, E. Talnishnikh and B. Blumich, *Magn. Reson. Imaging*, 2005, **23**, 383.
112 B. M. Weckhuysen, *Phys. Chem. Chem. Phys.*, 2003, **5**, 4351.
113 A. Urakawa and A. Baiker, *Topics in Catalysis*, 2009, **52**, 1312.
114 S. Mitchell, N.-L. Michels, G. Majano and J. Perez-Ramirez, *Curr. Opinion Chem. Eng.*, 2013, **2**, 304.
115 B. M. Weckhuysen, *Angew. Chem. Int. Ed.*, 2009, **48**, 4910.
116 A. A. Lysova, A. von Garnier, E. H. Hardy, R. Reimert and I. V. Koptyug, *Chem. Eng. J.*, 2011, **173**, 552.
117 I. V. Koptyug, A. V. Kulikov, A. A. Lysova, V. A. Kirillov, V. N. Parmon and R. Z. Sagdeev, *J. Am. Chem. Soc.*, 2002, **124**, 9684.
118 I. V. Koptyug, A. V. Kulikov, A. A. Lysova, V. A. Kirillov, R. Z. Sagdeev and V. N. Parmon, *Doklady Phys. Chem.*, 2002, **385**, 158.
119 I. V. Koptyug, A. V. Kulikov, A. A. Lysova, V. A. Kirillov, V. N. Parmon and R. Z. Sagdeev, *Chem. Sust. Dev.*, 2003, **11**, 109.
120 V. A. Kirillov and I. V. Koptyug, *Ind. Eng. Chem. Res.*, 2005, **44**, 9727.
121 I. V. Koptyug, A. A. Lysova, A. V. Kulikov, V. A. Kirillov, V. N. Parmon and R. Z. Sagdeev, *Appl. Catal. A: General*, 2004, **267**, 143.
122 I. V. Koptyug, A. A. Lysova, A. V. Kulikov, V. A. Kirillov, V. N. Parmon and R. Z. Sagdeev, *Magn. Reson. Imaging*, 2005, **23**, 221.
123 V. A. Kirillov, I. V. Koptyug, A. V. Kulikov, N. A. Kuzin, A. A. Lysova, A. B. Shigarov and V. N. Parmon, *Theor. Found. Chem. Eng.*, 2005, **39**, 24.
124 A. A. Lysova, I. V. Koptyug, A. V. Kulikov, V. A. Kirillov and R. Z. Sagdeev, *Topics in Catalysis*, 2009, **52**, 1371.
125 A. Ayude, J. Cechini, M. Cassanello, O. Martinez and P. Haure, *Chem. Eng. Sci.*, 2008, **63**, 4969.
126 W. Dietrich, L. Anadon, A. Sederman, L. Gladden and D. Agar, *Ind. Eng. Chem. Res.*, 2012, **51**, 1672.
127 B. Blumich, L. B. Datsevich, A. Jess, T. Oehmichen, X. Ren and S. Stapf, *Chem. Eng. J.*, 2007, **134**, 35.
128 L. Buljubasich, B. Blumich and S. Stapf, *J. Magn. Reson.*, 2011, **212**, 47.
129 L. Buljubasicha, B. Blumich and S. Stapf, *Chem. Eng. Sci.*, 2010, **65**, 1394.
130 D. A. Beauregard, P. Yong, L. E. Macaskie and M. L. Johns, *Biotechnol. Bioeng.*, 2010, **107**, 11.
131 S. Tsushima and S. Hirai, *Fuel Cells*, 2009, **9**, 506.
132 K. W. Feindel, S. H. Bergens and R. E. Wasylishen, *ChemPhysChem*, 2006, **7**, 67.
133 O. H. Han, *Progr. NMR Spectr.*, 2013, **72**, 1.
134 A. J. Sederman, M. D. Mantle, C. P. Dunckley, Z. Huang and L. F. Gladden, *Catal. Lett.*, 2005, **103**, 1.
135 E. H. L. Yuen, A. J. Sederman and L. F. Gladden, *Appl. Catal. A: General*, 2002, **232**, 29.

Downloaded from http://books.rsc.org/books/edited-volume/chapter-pdf/1688710/bk9781849739191-00001.pdf by guest on 03 October 2023

136 M. Kuppers, C. Heine, S. Han, S. Stapf and B. Blumich, *Appl. Magn. Reson.*, 2002, **22**, 235.
137 D. Weber, D. J. Holland and L. F. Gladden, *Appl. Catal. A: General*, 2011, **392**, 192.
138 S. B. Jaffe, *Ind. Eng. Chem., Process Des. Dev.*, 1976, **15**, 410.
139 J. Hanika, R. Lange and F. Turek, *Chem. Eng. Process.*, 1990, **28**, 23.
140 P. M. Haure, S. M. Bogdashev, M. Bunimovich, A. N. Stegasov, R. R. Hudgins and P. L. Silveston, *Chem. Eng. Sci.*, 1990, **45**, 2255.
141 O. Korup, S. Mavlyankariev, M. Geske, C. F. Goldsmith and R. Horn, *Chem. Eng. Proc.*, 2011, **50**, 998.
142 G. M. Carlomagno and G. Cardone, *Exp. Fluids*, 2010, **49**, 1187.
143 M. Simeone, L. Salemme and C. Allouis, *Int. J. Hydr. Energy*, 2008, **33**, 4798.
144 B. Li, K. Maruyama, M. Nurunnabi, K. Kunimori and K. Tomishige, *Ind. Eng. Chem. Res.*, 2005, **44**, 485.
145 B. Pinkerton and D. Luss, *Ind. Eng. Chem. Res.*, 2007, **46**, 1898.
146 B. Marwaha, S. Sundarram and D. Luss, *Chem. Eng. Sci.*, 2004, **59**, 5569.
147 J. Kopyscinski, T. J. Schildhauer, F. Vogel, S. M. A. Biollaz and A. Wokaun, *J. Catal.*, 2010, **271**, 262.
148 D. German, P. Chevallier, A. Laurent and H. Saint-Jalmes, *MAGMA*, 2001, **13**, 47.
149 W. Wlodarczyk, M. Hentschel, P. Wust, R. Noeske, N. Hosten, H. Rinneberg and R. Felix, *Phys. Med. Biol.*, 1999, **44**, 607.
150 B. Quesson, J. A. de Zwart and C. T. W. Moonen, *J. Magn. Reson. Imaging*, 2000, **12**, 525.
151 V. V. Zhivonitko, I. V. Koptyug and R. Z. Sagdeev, *J. Phys. Chem. A*, 2007, **111**, 4122.
152 I. V. Koptyug, A. V. Khomichev, A. A. Lysova and R. Z. Sagdeev, *J. Am. Chem. Soc.*, 2008, **130**, 10452.
153 A. A. Lysova, A. V. Kulikov, V. N. Parmon, R. Z. Sagdeev and I. V. Koptyug, *Chem. Commun.*, 2012, **48**, 5763.
154 V. Demas and P. J. Prado, *Concepts Magn. Reson.*, 2009, **34A**, 48.
155 *Single-Sided NMR*, ed. F. Casanova, J. Perlo and B. Blümich, Springer-Verlag, Berlin, Heidelberg, 2011.
156 A. J. Moule, M. M. Spence, S. Han, J. A. Seeley, K. L. Pierce, S. Saxena and A. Pines, *Proc. Natl. Acad. Sci. USA*, 2003, **100**, 9122.
157 C. Hilty, E. E. McDonnell, J. Granwehr, K. L. Pierce, S. Han and A. Pines, *Proc. Natl. Acad. Sci. USA*, 2005, **102**, 14960.
158 T. Z. Teisseyre, J. Urban, N. W. Halpern-Manners, S. D. Chambers, V. S. Bajaj, F. Svec and A. Pines, *Anal. Chem.*, 2011, **83**, 6004.
159 V. V. Zhivonitko, V.-V. Telkki, J. Leppaniemi, G. Scotti, S. Fransilla and I. V. Koptyug, *Lab Chip*, 2013, **13**, 1554.
160 Hyperpolarization Methods in NMR Spectroscopy. *Top. Curr. Chem.*, 2013, 338. Volume Editor: Lars Kuhn.
161 S. Mansson, E. Johansson, P. Magnusson, C.-M. Chai, G. Hansson, J. S. Petersson, F. Stahlberg and K. Golman, *Eur. Radiol.*, 2006, **16**, 57.
162 J. Kurhanewicz, D. B. Vigneron, K. Brindle, E. Y. Chekmenev, A. Comment, C. H. Cunningham, R. J. DeBerardinis, G. G. Green, M. O. Leach, S. S. Rajan, R. R. Rizi, B. D. Ross, W. S. Warren and C. R. Malloy, *Neoplasia*, 2011, **13**, 81.
163 B. M. Goodson, *J. Magn. Reson.*, 2002, **155**, 157.
164 T. G. Walker and W. Happer, *Rev. Mod. Phys.*, 1997, **69**, 629.
165 G. Navon, Y.-Q. Song, T. Room, S. Appelt, R. E. Taylor and A. Pines, *Science*, 1996, **271**, 1848.
166 G. E. Pavlovskaya, Z. I. Cleveland, K. F. Stupic, R. J. Basaraba and T. Meersmann, *Proc. Natl. Acad. Sci. USA*, 2005, **102**, 18275.

Downloaded from http://books.rsc.org/books/edited-volume/chapter-pdf/1688710/bk9781849739191-00001.pdf by guest on 03 October 2023

167 K. F. Stupic, Z. I. Cleveland, G. E. Pavlovskaya and T. Meersmann, *J. Magn. Reson.*, 2011, **208**, 58.
168 J. H. Ardenkjaer-Larsen, B. Fridlund, A. Gram, G. Hansson, L. Hansson, M. H. Lerche, R. Servin, M. Thaning and K. Golman, *Proc. Natl. Acad. Sci. USA*, 2003, **100**, 10158.
169 *Appl. Magn. Reson.*, 2012, **43**, issue 1–2, Special issue ''The Different Magnetic Resonance Communities Join Forces for Progress in DNP''.
170 *Phys. Chem. Chem. Phys.*, 2010, **12**, issue 22, Themed issue on dynamic nuclear polarization.
171 K. Golman, L. E. Olsson, O. Axelsson, S. Mnsson, M. Karlsson and J. S. Petersson, *Brit. J. Radiol.*, 2003, **76**, S118.
172 E. Terreno, D. D. Castelli, A. Viale and S. Aime, *Chem. Rev.*, 2010, **110**, 3019.
173 P. Bhattacharya, B. D. Ross and R. Bunger, *Exp. Biol. Med.*, 2009, **234**, 1395.
174 R. A. Green, R. W. Adams, S. B. Duckett, R. E. Mewis, D. C. Williamson and G. G. R. Green, *Progr. NMR Spectr.*, 2012, **67**, 1.
175 C. R. Bowers and D. P. Weitekamp, *J. Am. Chem. Soc.*, 1987, **109**, 5541.
176 J. Natterer and J. Bargon, *Progr. NMR Spectr.*, 1997, **31**, 293.
177 D. Canet, C. Aroulanda, P. Mutzenhardt, S. Aime, R. Gobetto and F. Reineri, *Concepts Magn. Reson.*, 2006, **28A**, 321.
178 K. V. Kovtunov, V. V. Zhivonitko, I. V. Skovpin, D. A. Barskiy and I. V. Koptyug, *Top. Curr. Chem.*, 2013, **338**, 123.
179 K. V. Kovtunov and I. V. Koptyug, *Magnetic Resonance Microscopy: Spatially Resolved NMR Techniques and Applications*, ed. S. Codd and J. D. Seymour, Wiley-VCH, Weinheim, 2008, 101–115.
180 S. B. Duckett and N. J. Wood, *Coord. Chem. Rev.*, 2008, **252**, 2278.
181 H. G. Niessen, D. Schleyer, S. Wiemann, J. Bargon, S. Steiner and B. Driessen-Holscher, *Magn. Reson. Chem.*, 2000, **38**, 747.
182 S. B. Duckett and R. E. Mewis, *Acc. Chem. Res.*, 2012, **45**, 1247.
183 I. V. Koptyug, K. V. Kovtunov, S. R. Burt, M. S. Anwar, C. Hilty, S. Han, A. Pines and R. Z. Sagdeev, *J. Am. Chem. Soc.*, 2007, **129**, 5580.
184 K. V. Kovtunov, V. V. Zhivonitko, A. Corma and I. V. Koptyug, *J. Phys. Chem. Lett.*, 2010, **1**, 1705.
185 I. V. Skovpin, V. V. Zhivonitko and I. V. Koptyug, *Appl. Magn. Reson.*, 2011, **41**, 393.
186 I. V. Skovpin, V. V. Zhivonitko, R. Kaptein and I. V. Koptyug, *Appl. Magn. Reson.*, 2013, **44**, 289.
187 K. V. Kovtunov, I. E. Beck, V. I. Bukhtiyarov and I. V. Koptyug, *Angew. Chem. Int. Ed.*, 2008, **47**, 1492.
188 K. V. Kovtunov, V. V. Zhivonitko, L. Kiwi-Minsker and I. V. Koptyug, *Chem. Commun.*, 2010, **46**, 5764.
189 D. A. Barskiy, K. V. Kovtunov, A. Primo, A. Corma, R. Kaptein and I. V. Koptyug, *ChemCatChem*, 2012, **4**, 2031.
190 V. V. Zhivonitko, K. V. Kovtunov, I. E. Beck, A. B. Ayupov, V. I. Bukhtiyarov and I. V. Koptyug, *J. Phys. Chem. C*, 2011, **115**, 13386.
191 K. V. Kovtunov, I. E. Beck, V. V. Zhivonitko, D. A. Barskiy, V. I. Bukhtiyarov and I. V. Koptyug, *Phys. Chem. Chem. Phys.*, 2012, **14**, 11008.
192 L.-S. Bouchard, S. R. Burt, M. S. Anwar, K. V. Kovtunov, I. V. Koptyug and A. Pines, *Science*, 2008, **319**, 442.
193 V. V. Zhivonitko, V.-V. Telkki and I. V. Koptyug, *Angew. Chem. Int. Ed.*, 2012, **51**, 8054.
194 V. V. Zhivonitko, K. V. Kovtunov, P. L. Chapovsky and I. V. Koptyug, *Angew. Chem. Int. Ed.*, 2013, **52**, 13251.

Downloaded from http://books.rsc.org/books/edited-volume/chapter-pdf/1688710/bk9781849739191-00001.pdf by guest on 03 October 2023

195 M. Carravetta, O. G. Johannessen and M. H. Levitt, *Phys. Rev. Lett.*, 2004, **92**, 153003-1.
196 M. B. Franzoni, L. Buljubasich, H. W. Spiess and K. Munnemann, *J. Am. Chem. Soc.*, 2012, **134**, 10393.
197 W. S. Warren, E. Jenista, R. T. Branca and X. Chen, *Science*, 2009, **323**, 1711.
198 P. Ahuja, R. Sarkar, S. Jannin, P. R. Vasos and G. Bodenhausen, *Chem. Commun.*, 2010, **46**, 8192.
199 G. Pileio, S. Bowen, C. Laustsen, M. C. D. Tayler, J. T. Hill-Cousins, L. J. Brown, R. C. D. Brown, J. H. Ardenkjaer-Larsen and M. H. Levitt, *J. Am. Chem. Soc.*, 2013, **135**, 5084.
200 I. I. Koptyug, A. A. Lysova, G. A. Kovalenko, L. V. Perminova and I. V. Koptyug, *Appl. Magn. Reson.*, 2010, **37**, 483.
201 J. S. McLean, O. N. Ona and P. D. Majors, *ISME J.*, 2008, **2**, 121.
202 A. C. Humphries, I. P. Mikheenko and L. E. Macaskie, *Biotechnol. Bioeng.*, 2006, **94**, 81.
203 K. P. Nott, F. P. Heese, M. Paterson-Beedle, L. E. Macaskie and L. D. Hall, *Can. J. Chem. Eng.*, 2005, **83**, 68.

Downloaded from http://books.rsc.org/books/edited-volume/chapter-pdf/1688710/bk9781849739191-00001.pdf by guest on 03 October 2023